Physics of Fluids

Hydroplastic response of a square plate due to impact on calm water

Cite as: Phys. Fluids **32**, 082103 (2020); https://doi.org/10.1063/5.0013858
Submitted: 14 May 2020 . Accepted: 14 July 2020 . Published Online: 06 August 2020

B. C. Abrahamsen, H. S. Alsos, V. Aune, E. Fagerholt, O. M. Faltinsen, and Ø. Hellan

Hydroplastic response of a square plate due to impact on calm water

Cite as: Phys. Fluids 32, 082103 (2020); doi: 10.1063/5.0013858
Submitted: 14 May 2020 • Accepted: 14 July 2020 •
Published Online: 6 August 2020

View Online Export Citation CrossMark

B. C. Abrahamsen,[1,a)] H. S. Alsos,[1] V. Aune,[2,3] E. Fagerholt,[2] O. M. Faltinsen,[4] and Ø. Hellan[1]

AFFILIATIONS

[1] SINTEF Ocean, Otto Nielsens veg 10, 7052 Trondheim, Norway
[2] NTNU, Structural Impact Laboratory (SIMLab), Department of Structural Engineering, Richard Birkelands veg 1B, 7034 Trondheim, Norway
[3] NTNU, Centre for Advanced Structural Analysis (CASA), Richard Birkelands veg 1B, 7034 Trondheim, Norway
[4] NTNU, Centre for Autonomous Marine Operations and Systems (AMOS), Otto Nielsens veg 10, 7052 Trondheim, Norway

[a)] **Author to whom correspondence should be addressed:** bjornchristian.abrahamsen@sintef.no

ABSTRACT

This paper investigates large, plastic deflections of a square plate due to impact on calm water. Most research in the area has examined linear elastic structural responses to such impact, but hydrodynamic responses during large, plastic deformations of engineering structures remain under-explored. A setup for an experimental drop test was designed for this purpose with equal emphasis on the hydrodynamical and structural mechanical aspects. Dual cameras were used to monitor the deforming plate from above during impact, and its deformation was tracked using a three-dimensional digital image correlation technique. The complex hydrodynamics of the impact were captured using a high-speed camera from below. The experimental results for flat impact showed a large air pocket under the deforming plate. The material properties of the plate were documented through separate tests. Hydroelastic theories were offered to account for large deformations and validated against the experimental results. Analytical hydroplastic theory shows that the maximum deflection is approximately equal to the velocity of impact times the square root of the ratio of the added mass to the plastic membrane capacity of the plate. An important source of error between the theory and the experiments was the effect of deceleration of the drop rig on deflection of the plate. This error was estimated using direct force integration and Wagner's theory.

I. INTRODUCTION

Understanding fluid structure interaction during violent wave impact is important for the appropriate design of ships and ocean structures. The slamming phenomenon is characterized by large, local pressures of short duration. This study considers the problem where a flat plate is dropped onto a flat free surface. This is an idealized slamming impact to study details of the slamming phenomenon. A large amount of research has considered the slamming of rigid structures on water. Wagner[1] derived a slamming theory using incompressible potential flow while neglecting air flow. Other studies have considerably extended the theoretical understanding of slamming pressures, such as those by Korobkin,[2,3] and Zhao and Faltinsen.[4] Early work by Chuang,[5] Verhagen,[6] and Koeller and Kettleborough[7] considered flat impact between a nearly rigid plate and water and showed experimentally that the traditional theory proposed by Wagner[1] is not valid when the plate is parallel to the calm free surface. In this case, air is trapped between the plate and the free surface and dramatically alters the flows of air and water. Other research has revealed different aspects of the flow physics of a nearly rigid plate during flat impact on water. Mayer and Krechetnikov[8] studied the cushion of air trapped under the plate and jetting occurring at the plate edges, called ejecta, using both mathematical analysis and advanced particle image velocimetry (PIV) measurements.

The elastic response of a wedge consisting of two Euler beams exposed to slamming has been studied by many researchers. Lu *et al.*[9] coupled a nonlinear boundary element method in the water domain with a finite element discretization of the structure. Khabakhpasheva and Korobkin[10] studied the same problem but expressed beam deflection as the sum of normal modes and considered different simplifications of the problem. Shams *et al.*[11] also studied an elastic wedge consisting of two Euler beams and considered both the problem when the wedge entered and exited out of the water.

Okada and Sumi[12] studied impact pressures during a hydroelastic drop test of a half-wedge. The pressures and the strains were measured during the impact. The variation in the deadrise angle from 4° to 0° showed a transition from the Wagner type of impact with traveling jets to that of a trapped air cushion under the plate without jet formation. The local pressure under the plate was sensitive, while the maximum strain on the plate was insensitive to variations in the deadrise angle. A similar observation was made by Faltinsen *et al.*,[13] who studied elastic deformations in a plate strip during drop tests on waves with different radii of curvature. The results showed that the maximum strains in the plate were not sensitive to whether it was dropped on flat water or on a wave with a curvature radius 10 times longer than the beam length. Faltinsen[14] compared the results from the drop tests in Ref. 13 with a simplified theory where the impact was divided into two stages. The first stage, called the structural inertial phase, was very short. In it, the hydrodynamic load was balanced by inertial forces. At the end of this stage, the spatially averaged structural velocity was equal to the impact velocity of water. Following the structural inertial phase was a free vibration phase, where the plate oscillated with its wet natural period. Korobkin[15] provided a complete mathematical model of the problem studied by Faltinsen *et al.*[13] and commented on the validity of impulse response assumption in Ref. 14.

Yu *et al.*[16,17] recently extended the ideas in Ref. 14 by analyzing the nonlinear and plastic structural responses of a stiffener with an associated plate flange. The method they used separates the response into a structural inertial phase and a free deflection phase that accounts for structural nonlinearities. The free deflection phase was divided into a traveling hinge stage (stage 1), a stationary hinge stage (stage 2), and a pure tension stage (stage 3). The results of this method compared well to those of nonlinear finite element simulations.

Faltinsen[18] also developed a hydroelastic mathematical model that combined orthotropic plate theory with a Wagner-type hydrodynamic model. The results showed that the importance of hydroelasticity depends on the ratio of the duration of application of load to the natural period of the structure. The duration depends on the impact velocity as well as the angle between the free surface and the structure. An important observation regarding the theory in Ref. 18 is that for relevant impact velocities taken from steep and breaking waves, and the relevant dimensions of stiffened panels used in ocean structures, it predicts stresses that exceed the yield stress.

Many researchers have studied the hydroelastic problem, but the phenomenon of large, nonlinear, and plastic deformations has received very limited attention. This paper examines the large, plastic deformation of a plate during slamming impact with a calm free surface of water. The requisite drop tests could not be carried out at full scale for practical and financial reasons, which means that the structure needed to be scaled down and simplified. To scale the model tests, it is useful to derive simplified analytical formulas that clearly identify the main physical parameters of the problem at hand. For this purpose, the theory by Faltinsen[14] is extended to account for the large and plastic deformations of a plate during flat impact on calm water. This analytical hydroplastic theory is presented in Sec. II. The model is subsequently compared with the experimental results in Sec. XI.

The aim of the model test developed here is to measure large deformations in a plate hitting a flat free surface with nearly constant impact velocity. The three-dimensional (3D) digital image correlation (3D-DIC) technique is used to measure the deformation of the plate. An important feature of the test setup was therefore to allow for optical measurements of the plate from above. This test setup is presented in Sec. III.

Many researchers have studied the hydroelastic response of Euler beams. In this case, the only material properties required are the elastic modulus and the density of the beam. When large plastic deformations are considered, an accurate relationship between stress and strain is required, and an accurate material model needs to be specified. Section IV presents separate uniaxial stress tests of the material of the plate that are used to establish an accurate description of it. Section V presents the results of the drop tests, and Sec. VI discusses the accuracy of the 3D-DIC measurements and repetition error in deflections of the plate. Section VII presents the estimated impact velocity based on the principle of energy conservation, which is compared against the measurements in Sec. VIII. Error analysis is important to assess the accuracy of experiments. The error analysis of the experimental setup here used both mathematical and experimental methods. An important source of bias was the way in which the deceleration of the entire rig during impact affected the deformation of the plate. This error is investigated with a separate mathematical model in Sec. IX. Section X presents nonlinear finite element analysis (FEA) to provide an estimate of the effect of the strain rate on the maximum deflections of the plate, and Sec. XI presents comparisons between the calculated and measured deflections of the plate.

II. HYDROPLASTIC THEORY BASED ON INITIAL VELOCITY CONDITIONS

Figure 1 shows the problem of a rectangular surface impacting a calm free surface. The surface represents the wetted area of a structure with a flat, horizontal bottom, with a flexible plate mounted in the middle (gray area). Hydroplastic theory uses the same overall

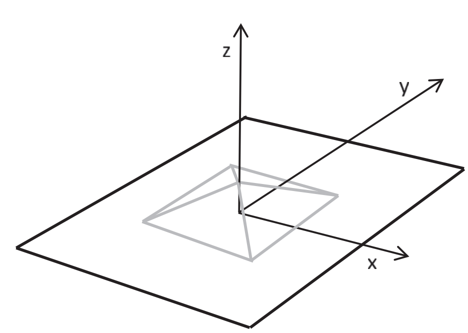

FIG. 1. Schematic of the rectangular surface impacting a calm free surface. The gray lines indicate the theoretical deformation pattern of the plate.

approach as for the hydroelastic beam studied by Faltinsen.[14] Hence, the impact is divided into a structural inertial phase and a free vibration phase. During the structural inertial phase, a large load occurred over a short duration. The stiffness of the structure was negligibly small, and the load was balanced by the inertia of the plate. The mathematical analysis in Ref. 14 shows that the spatially averaged velocity of the plate is approximately equal to the impact velocity at the end of the structural inertial phase. For the plate studied here, the mode of deformation is assumed to be shaped as a pyramid. The displacement field $w(x, y)$ is expressed as

$$w = w_1 \bar{N}(x,y) = w_1 \begin{cases} 1 - \frac{|x|}{L_p}, & |x| \geq |y| \\ 1 - \frac{|y|}{L_p}, & |x| < |y|, \end{cases} \tag{1}$$

where L_p is half the width of the square plate and $\bar{N}(x, y)$ is the shape function. The initial velocity of the plate in the free vibration stage is

$$\int_S \dot{w}\bar{N}(x,y)dS = \int_S V\bar{N}(x,y)dS, \tag{2}$$

where V is the impact velocity, which is assumed to be constant during impact, and S is the surface of the flexible plate. Equation (2) states that the spatially averaged plate velocity is equal to the impact velocity. The initial condition for the free vibration stage is

$$\dot{w}_1(t = 0) = 2V. \tag{3}$$

Furthermore, the displacement at the beginning of the free vibration stage is assumed to be zero. The theory derived should describe the large, plastic deformations of the plate. A practical theory for this purpose is the rigid plastic theory proposed by Jones,[19] whereby an approximate formula for the deflection of a plate undergoing large deformations is given as

$$\int_S (p - \mu\ddot{w})\dot{w}dS = \sum_{m=1}^{N_m} \int_{lm} (Nw - M)\dot{\theta}_m dl_m, \tag{4}$$

where w is the deflection of the plate, p is pressure on its surface, μ is the mass per unit area of the plate, and l_m is the length of the hinge line m. The right-hand side of Eq. (4) sums structural resistance along the number of hinge lines N_m. N is the membrane force per unit length, M is the bending moment per unit length, and $\dot{\theta}_m$ is the relative rate of angular rotation across the hinge. The underlying assumptions in Eq. (4) are as follows: (1) the material is perfectly plastic, (2) in-plane displacements are much smaller than displacements normal to the plate surface, (3) plastic collapse is time independent and does not allow for traveling hinges, and (4) the shape of the displacement field is equal to the velocity profile of static collapse. The velocity potential of water on the surface of the plate due to the motion of the mode is written as $\varphi = \dot{w}_1\bar{\varphi}(x, y)$. Figure 1 shows the boundary value problem for $\bar{\varphi}(x, y)$. On the free surface, $\bar{\varphi} = 0$, while on the rigid part of the structure, $\partial\bar{\varphi}/\partial z = 0$. The gray lines indicate the shape of the pyramid deflection mode of the flexible plate, where the boundary condition is $\partial\bar{\varphi}/\partial z = \bar{N}(x, y)$. Pressure acting on the plate due to its acceleration is $p = -\rho\ddot{w}_1\bar{\varphi}(x, y)$. The hydrodynamic force due to the acceleration of the plate in Eq. (4) is

$$\int_S p\dot{w}dS = -\rho\ddot{w}_1\dot{w}_1 \int_S \bar{\varphi}(x,y)\bar{N}(x,y)dS = -\ddot{w}_1\dot{w}_1 A. \tag{5}$$

Here, A is the coefficient of added mass due to unit amplitude oscillations of the pyramid mode. The mass term in Eq. (4) is

$$\int_S \mu\ddot{w}\dot{w}dS = \frac{2}{3}\mu L^2\ddot{w}_1\dot{w}_1 = M_s\ddot{w}_1\dot{w}_1. \tag{6}$$

Assuming that the four edges of the plate are clamped, the right-hand side of Eq. (4) is, according to Jones,[20] equal to

$$16M_0\left[1 + \frac{1}{3}\left(\frac{w_1}{h}\right)^2\right]\dot{w}_1 \quad \text{for} \quad \frac{w_1}{h} < 1 \tag{7}$$

and

$$16M_0\left(\frac{w_1}{h} + \frac{1}{3}\frac{h}{w_1}\right)\dot{w}_1 \quad \text{for} \quad \frac{w_1}{h} \geq 1, \tag{8}$$

where $M_0 = \sigma_0 h^2/4$ is the plastic moment capacity of the plate, σ_0 is the effective yield stress of the material composing it, and h is the thickness of the plate. Furthermore, if the deflection of the plate is large compared to its thickness, Eq. (8) is equal to $4N_0 w_1\dot{w}_1$. Here, $N_0 = \sigma_0 h$ is the membrane capacity of the plate. Assuming large deformations, Eq. (4) can be written as

$$[A + M_s]\ddot{w}_1 + 4N_0 w_1 = 0. \tag{9}$$

Equation (9) is valid only if $\dot{w}_1 > 0$ because the theory assumes plastic behavior of the plate. The solution to Eqs. (9) and (3) is

$$w_1 = \bar{w}_1 \sin(\omega t) \quad t < T_r. \tag{10}$$

Here, $\omega^2 = 4N_0/(A + M_s)$. The deflection maximum is

$$\bar{w}_1 = V\sqrt{\frac{M_s + A}{N_0}}. \tag{11}$$

T_r is the rise time of the midpoint deflection from zero to its maximum value. Hence, $T_r = \pi/(2\omega)$ and

$$T_r = \frac{\pi}{2}\sqrt{\frac{M_s + A}{4N_0}}. \tag{12}$$

The plate deflection according to Eqs. (10) and (11) is referred to as the "analytical hydroplastic solution" throughout this paper.

III. SETUP OF THE DROP TEST

Figure 2 shows the principle of the drop test. A rotating arm was mounted on a hinge on the left side. The arm was first rotated counterclockwise and then released before the box fell freely until it hit the surface of the calm water. The pivot point of the hinge was defined as the origin for the $\tilde{x}$, $\tilde{y}$, $\tilde{z}$ coordinate system. The center of the undeformed plate was the origin for the body-fixed coordinate system x, y, z. An open box was attached to the end of the arm; its underside was rectangular, with dimensions of 344×500 mm^2.

The box was left open to allow for a clear view of the deformation of the plate using two Phantom v2511 high-speed cameras operating at 37 kHz. All plates were spray-painted with a speckle pattern to enable 3D-DIC measurements. The plate and the speckle

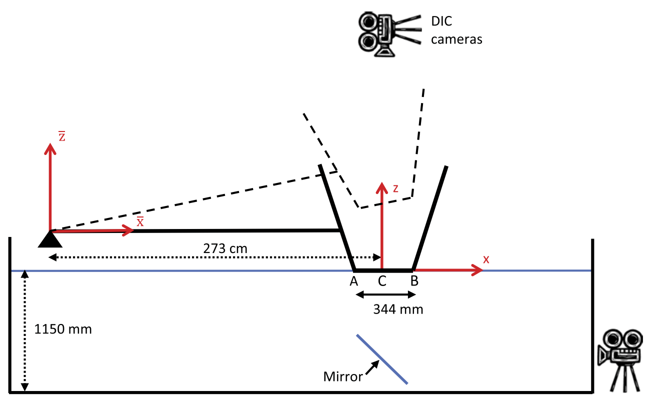

FIG. 2. Drop test designed with an open structure to enable a clear view of the plate during the impact. The motion of the plate was captured from images obtained using the 3D-DIC technique. The hydrodynamic flow was documented with a high-speed camera that filmed the plate from below.

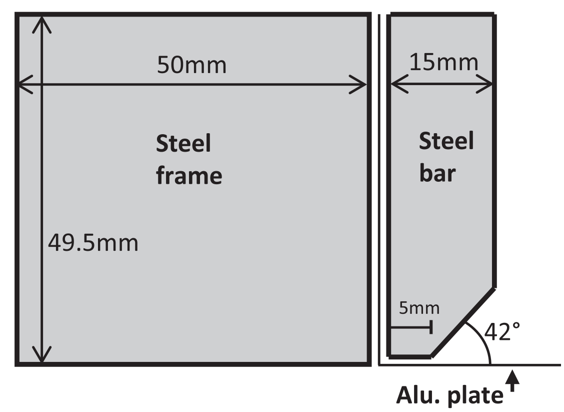

FIG. 4. The drawing shows a cross section of the steel frame, steel bar, and aluminum plate.

pattern are shown in Fig. 3(b). The 3D-DIC technique as implemented in the eCorr software[21] was used to track deformations of the plate. Details of this technique have been described by Fagerholt.[22] To isolate deflections of the plate from the rigid-body motion of the frame, selected parts of the frame were observed using the DIC cameras. A set of sticker-markers on the frame allowed for point-wise 3D-DIC, providing for rigid-body measurements of the frame during the test.

One high-speed camera was installed on the floor outside the basin to study the hydrodynamics of the impact. It filmed the impact from below the plate through a mirror at a frequency of 3 kHz. The dropped box was equipped with accelerometers to monitor the motion/rotation of the rigid body. The accelerometers were sampled at a frequency of 19.2 kHz.

The photograph in Fig. 3(a) shows the steel box at the bottom, and photograph (b) shows the steel frame that held the flexible plate. The bottom of the yellow box had an opening where the steel frame containing the flexible plate was installed. The frame consisted of four equal large steel parts with a rectangular cross section of 49.5×50 mm^2. These parts were screwed on top of one another to form a stiff square frame. The area inside the frame was used to fit the 230×230 mm^2 aluminum sections. These deformable sections were clamped between the inside of a steel frame and four thick steel bars using 12 screws (M12 × 1.75). Figure 4 shows details of the connection between the plate and the frame. The steel bars were tapered from 15 mm to 5 mm toward the lower edge supporting the aluminum box. The plate was assumed to be fixed at the edge of the bar toward the center of the plate. This means that the plate width ($2L_p$) was set to 220 mm in all calculations.

The drop test was designed to study the deformation in steel plates caused by slamming waves in a simplified manner. Experience from model tests of large ocean structures shows that the largest slamming loads on a typical 3×3 m^2 structure during a 100-yr storm comes from high and steep waves. These waves strike the side of the structure with a typical velocity of about 15 m/s. To achieve this velocity, a drop height of more than 10 m is required. This was not possible here, and the authors decided to perform the experiment at a smaller scale.

To model the nonlinear structural response of the plate when undergoing large deformations, Eqs. (10) and (11) suggest that the membrane capacity of the plate should be scaled correctly. The impact velocity V in Eq. (11) is a factor $\sqrt{\lambda}$ smaller for the model than in full scale, where λ is the geometrical scaling ratio. By inserting full scale values in Eq. (11) and dividing it with parameters of the

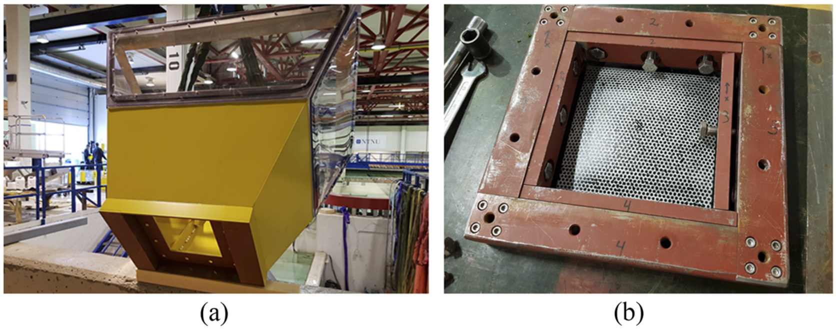

FIG. 3. (a) Photograph of the box from below. (b) Photograph of the frame after a test during the unmounting of the deformable aluminum section.

model scale, the scaling of the membrane capacity is

$$\frac{N_{0p}}{N_{0m}} = \frac{\bar{w}_{1m}}{\bar{w}_{1p}} \frac{V_p}{V_m} \sqrt{\frac{A_p}{A_m}} = \mathrm{r}\lambda^2, \tag{13}$$

where the structural mass M is neglected as it is much smaller than the added mass A. The subscript p denotes values of the prototype (full scale) and m denotes those of the model scale.

This scaling was motivated by the impressive comparisons in terms of plate deformations and stresses between experiments and the hydroelastic theory in Ref. 14. The aim was to obtain geometrically scaled plate deformations. The accuracy of the scaling strategy is discussed further in Sec. XI.

The membrane capacity is the product of the thickness of the plate and the yield strength. To achieve a correctly scaled plate, a thin metal with low yield strength was needed. A 0.6-mm-thick aluminum plate was used here, manufactured from low-strength, strain-hardened, and cold-rolled sheets of the commercial alloy EN AW 1050A-H111. The nominal chemical composition of the material was 0.06% Si, 0.29% Fe, 0.01% Ti, and 99.64% Al.

IV. MATERIAL TEST OF ALUMINUM PLATE

To accurately identify the relationship between stress and strain, five material uniaxial tensile tests were carried out. Three test specimens were cut from the plate material in the direction of rolling, and two specimens were cut in the orthogonal direction. Two-dimensional digital image correlation (2D-DIC)[22,23] was used to measure displacements. Figure 5 shows the nominal and true stress–strain curves. The nominal stress σ_e and strain ε_e are given by

$$\sigma_e = \frac{F}{A_0}, \ \varepsilon_e = \frac{u}{L_0}, \tag{14}$$

where F is the pull force, A_0 is the initial cross-sectional area in the gauge region, u is the elongation, and L_0 is the initial specimen length. The true stress σ and the true strain ε were determined using the following respective equations: $\sigma = \sigma_e(1 + \varepsilon_e)$ and $\varepsilon = \ln(1 + \varepsilon_e)$. The results showed that the aluminum was slightly anisotropic in terms of flow stress, since the magnitudes of the force and stress levels were slightly lower orthogonally than in line with the rolling direction.

To facilitate accurate finite element analysis (FEA) of the plate, it was necessary to establish a suitable material model for this aluminum alloy. The characteristics for the sheet metal applied in the tests featured isotropic plastic properties with strong rate defects. Hence, the behavior of the plastic material was described using the modified Johnson–Cook model (*MAT_107 in LS-DYNA;[24] see also Ref. 25 for further details). This model accounts for large plastic strains and high strain rates. The constitutive equation reads

$$\sigma_{eq} = \left[\sigma_0 + \sum_{i=1}^{2} Q_i(1 - \exp(-C_i p))\right]\left[1 + \dot{p}^*\right]^{\bar{c}}\left[1 - T^{*m}\right]. \tag{15}$$

Here, σ_{eq} is the equivalent von Mises stress and p is the equivalent plastic strain. The yield stress, σ_0 = 27 MPa, is the stress corresponding to 0.2% plastic deformation. The Voce parameters Q_1 = 23.8 MPa, Q_2 = 55.8 MPa, C_1 = 46.7, and C_2 = 4.2 were estimated using the method of least squares. The constant of strain rate sensitivity $\bar{c}$ was assumed to be 0.014 (see Refs. 26 and 27). $m = 1$ was a material constant controlling temperature-softening in the material. The dimensionless plastic strain rate was $\dot{p}^* = \dot{p}/\dot{p}_0$, and $\dot{p}_0 = 5 \times 10^{-4}\left[\mathrm{s}^{-1}\right]$ was the user-defined reference strain rate. The homologous temperature was defined as $T^* = (T - T_r)/(T_m - T_r)$, where T is the absolute temperature, T_r = 293 K is the

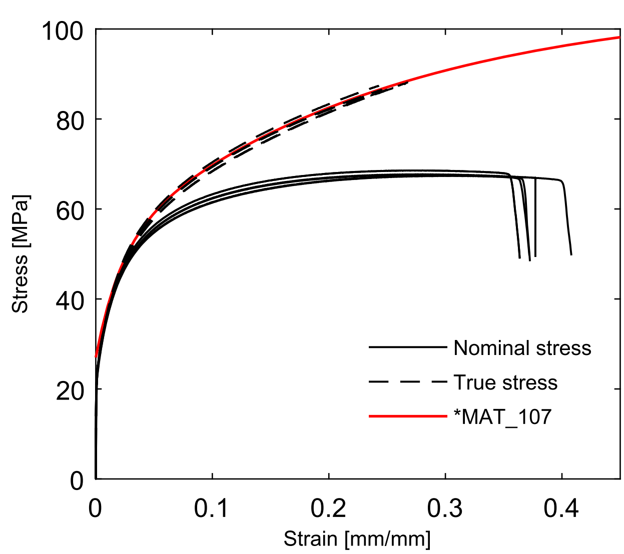

FIG. 5. Nominal and true stress–strain curves from uniaxial tensile tests cut from the material of the plate: aluminum alloy EN AW 1050A-H111.

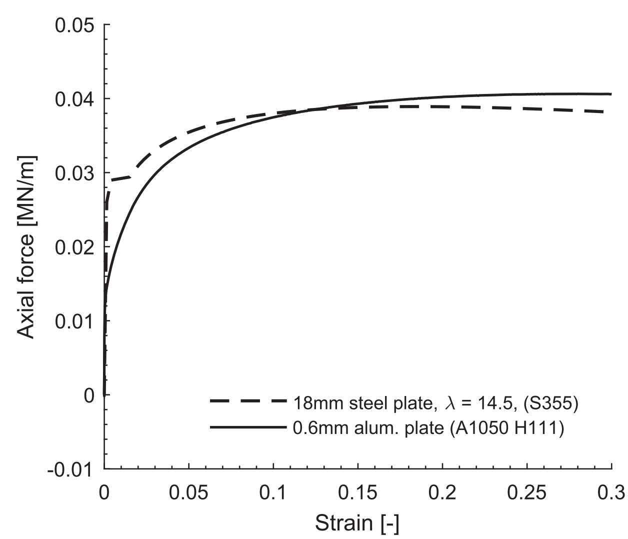

FIG. 6. Membrane force as a function of strain. The prototype material was an 18-mm steel (S355) plate scaled to a model scale of 14.5 according to scaling laws based on analytical hydroplastic theory. The model material was a 0.6-mm-thick aluminum plate (EN AW 1050A-H111).

ambient temperature, and T_m = 893 K is the melting temperature of the material. The following physical constants were required to complete the model of the material (see Ref. 28): Young's modulus E = 70 GPa, Poisson's ratio ν = 0.3, material density ρ = 2700 kg/m^3, thermal expansion coefficient α = 2.3 × 10^{-5}, specific heat C_p = 910 J/kg K, and Taylor–Quinney coefficient χ = 0.9. Figure 5 shows that the calibrated material model compared well with measurements of the uniaxial tension test. This material model was used in the FEA of the plate described in Sec. X.

Figure 6 shows the axial force in the aluminum plate as a function of strain in a uniaxial tensile test (black curve). The dashed curve shows the axial force of steel S355 as specified in Ref. 29 at a scale of 1:14.5 using Eq. (13). The plot shows that the 0.6-mm-thick aluminum plate was a rough model of an 18-mm-thick steel plate of type S355 when the response of the plate is dominated by membrane forces.

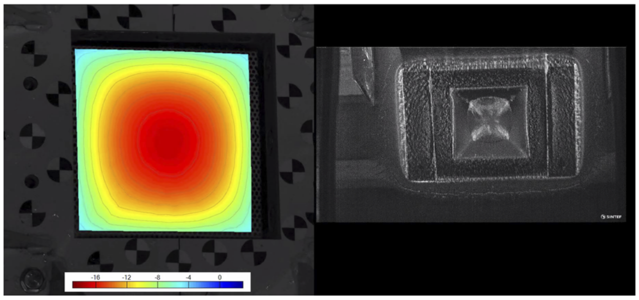

FIG. 7. Synthesized video showing images from the camera mounted above the plate and the camera filming the plate from below through the mirror. The colored plot on the left shows the deflection of the plate extracted using the 3D-DIC technique, and the image to the right shows details of the flows of air and water beneath the plate during test 1. Multimedia view: https://doi.org/10.1063/5.0013858

V. RESULTS OF THE DROP TEST

Table I shows the test program for the drop tests. They were carried out at different drop heights and angles varying from 0° to 4°. The drop height refers to the vertical distance between point A and the free surface in Fig. 1. The angle in Table I is the angle between the underside of the box and the calm free surface when the box touched the free surface. The angle is positive in the clockwise direction.

Figure 7 shows a synthesized video of test 1. The left half shows images recorded from the top. The color plot shows the deflection of the plate measured using the 3D-DIC technique. The right half of the video shows images recorded from the high-speed video filmed from below.

Figure 8 shows the deformation in the center of the plate as a function of time during test 1 at a drop height of 443 mm. The angle between the plate and the calm free surface was 0°. The two main characteristics of the deformation were as follows: (1) There was a short period from 0 ms to 5 ms, where the plate deformed rapidly until the maximum deformation was reached. This period is called the "rapid deflection" stage of impact. (2) Once the maximum deflection had been reached, the plate deflected back downward before it deflected upward again. We call this stage the "bounce back" stage.

TABLE I. Drop test program.

Test no.	Angle (deg)	Height (mm)
1	0	443
2	0	443
3	0	443
4	0	118
5	0	222
6	0	778
7	0	778
8	0	778
9	4	444

Figure 9 shows high-speed images recorded from underneath the plate during the rapid deflection stage. The image sequence started when there was no visible deformation in the plate, and no visible interaction between the escaping air from the front of the plate and the water. In the second image (−0.5 ms), the air flow created ripples on the surface of water. In the time between images 2 and 4, an air pocket formed. Image 4 (0.8 ms) shows an air pocket covering large parts of the aluminum plate. It is evident that deformations of the plate had begun by this time.

It is important to compare the physics of the air entrapment process with that of the air trapped under a nearly rigid plate. Verhagen[6] observed that air flow has a non-negligible influence on the shape of the free surface when the distance between the body and the free surface is short. Consequently, the level of water is

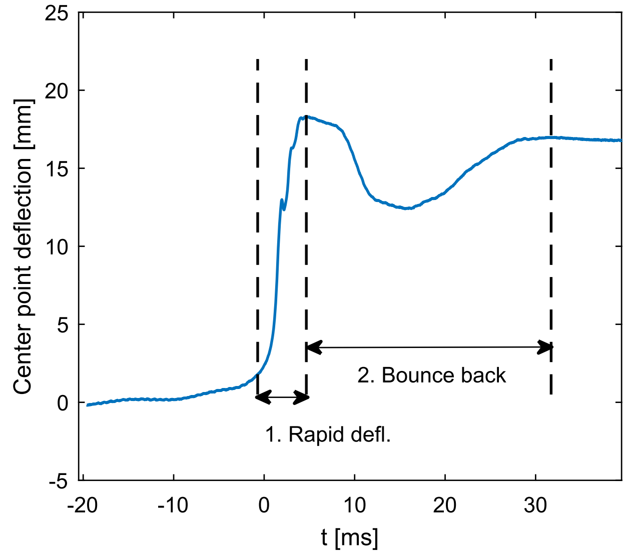

FIG. 8. Time history of deformation in the center of the plate as measured by the 3D-DIC for test 1 (drop height of 443 mm).

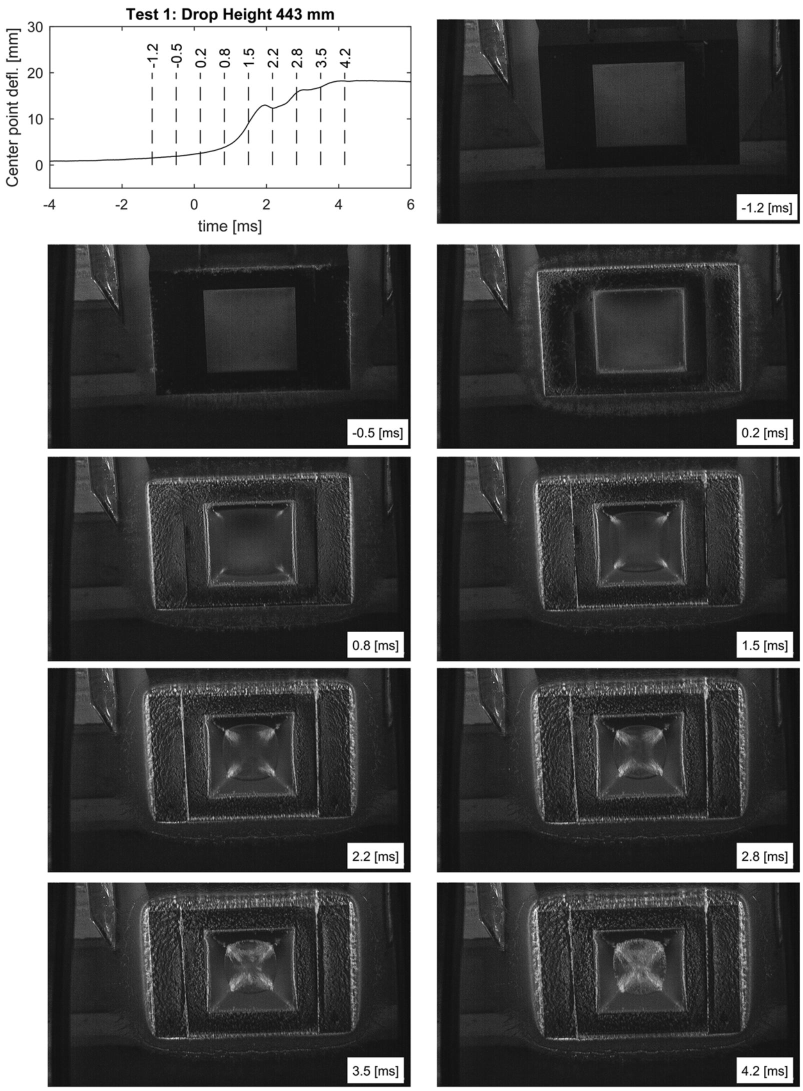

FIG. 9. High-speed images recorded at 3 kHz, showing flat impact at a drop height of 443 mm (test 1). The image sequence shows the time of initial contact between the underside of the box and water and through to the stage of rapid deformation of the plate ending at the maximum.

raised at the edges of the plate, causing a thin air cushion between the plate and the free surface. In the case of a nearly rigid plate, this air cushion covered the entire area of the plate before breaking down into bubbles. Watanabe *et al.* [30] experimentally studied the air entrapment and leakage using a transparent ship model and described the air entrapment and leakage for a real ship shape in a seaway.

To study the influence of the stiffness of the plate on air entrapment, separate drop tests were carried out with a much stiffer 1 mm steel plate. Figure 10(a) shows the air–water mixture under the plate when dropped from a height of 21 mm. Note that the drop height was lower than for the 0.6-mm aluminum plate. The duration between the photographs in Figs. 10(a) and 10(b) was 8 ms, and the images show a more chaotic air–water mixture than in the case of the 0.6-mm aluminum plate. In this case, less air was trapped into different sizes of smaller air pockets during the slam. This suggests that the entrapment of the air pocket in the experiments was influenced by the stiffness of the plate. Furthermore, for the 0.6-mm-thick aluminum plate, the membrane capacity was scaled appropriately, while the elastic bending stiffness was not

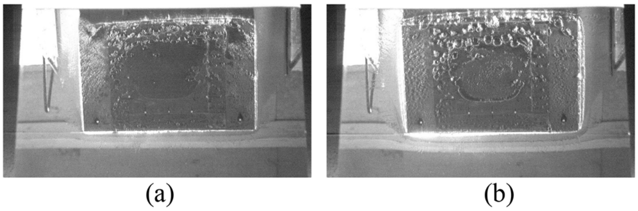

FIG. 10. Photographs of the air–water mixture during the drop test with a 1 mm steel plate. The time between photographs (a) and (b) was 8 ms.

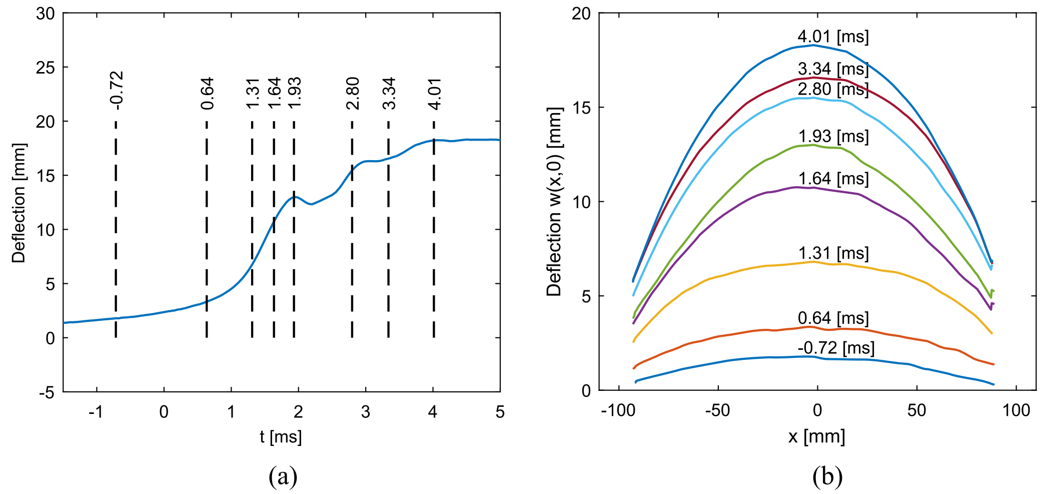

FIG. 11. (a) Deflection of the center of the plate during the "rapid deflection" stage. (b) Profiles of the deflection along the center line y = 0. The drop height was 443 mm (test 1).

considered. If the elastic bending stiffness per unit width of an 18-mm-thick steel plate is scaled correctly, the bending stiffness should be $EI/(\lambda^4 r)$ = 2.25 N m, where E = 210 GPa is the elasticity modulus and $I = h^3/12$ is the second moment of the area of the plate per unit width. The bending stiffness of the tested 0.6-mm-thick aluminum plate was 1.3 N m and 17.5 N m for the 1 mm steel plate. This means that the 0.6-mm aluminum plate had a lower bending stiffness, while the 1 mm steel plate had a much larger bending stiffness than a properly scaled 18-mm steel plate. This stiffness error was considered to affect the formation of the air pocket. Hydrodynamical aspects of scaling are discussed in Sec. XI.

Figure 11(a) shows the deflection at the center of the plate as a function of time during the "rapid deflection" stage, and Fig. 11(b) shows deformation profiles along the center line (y = 0). The times of these profiles are indicated in Fig. 11(a).

Figure 12(a) shows the deflection at the center of the plate during its "bounce back" stage. The duration of this phenomenon was ~20 ms. Figures 12(b) and 12(c) show profiles of the deformation along the center line of the plate (y = 0). Plot (b) shows the deformation down from the maximum deflection, while plot (c) shows the plate as it was pushed up again. The deformed shape of the plate during this stage was almost constant in space, which suggests large deformations near the boundaries. The measurement shows that the plate deflected to −4 mm near its left edge.

Figure 13 shows high-speed images in the same period. The plate buckled toward the upper part of the image. The positive x axis is directed downward in the figure. The buckled part of the

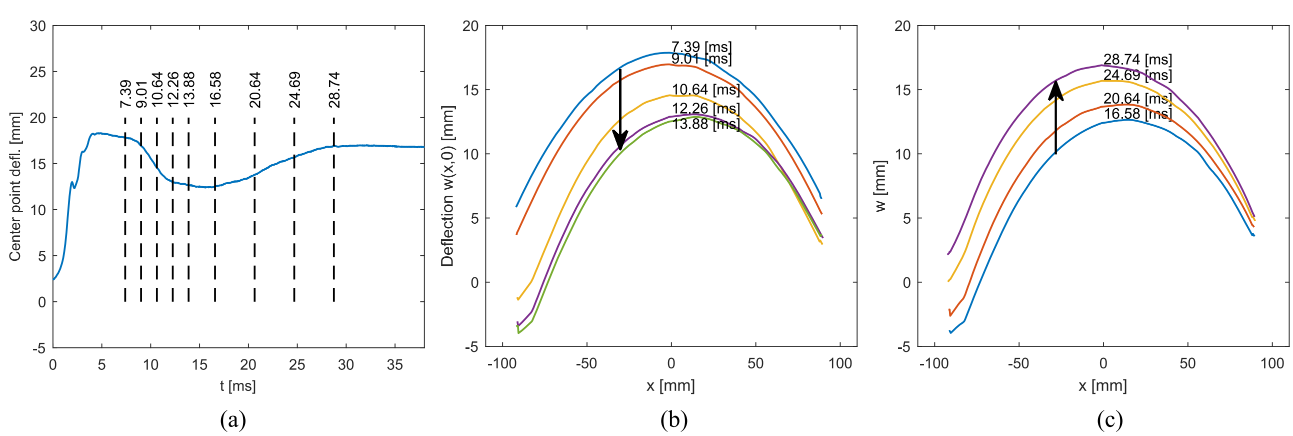

FIG. 12. Measured deflection of the plate during the "bounce back" stage of the impact. Drop height was 443 mm (test 1). (a) Time history of deformation at the center of the plate. [(b) and (c)] Deformation profiles along the center line y = 0 when (b) pushed down and (c) pushed up.

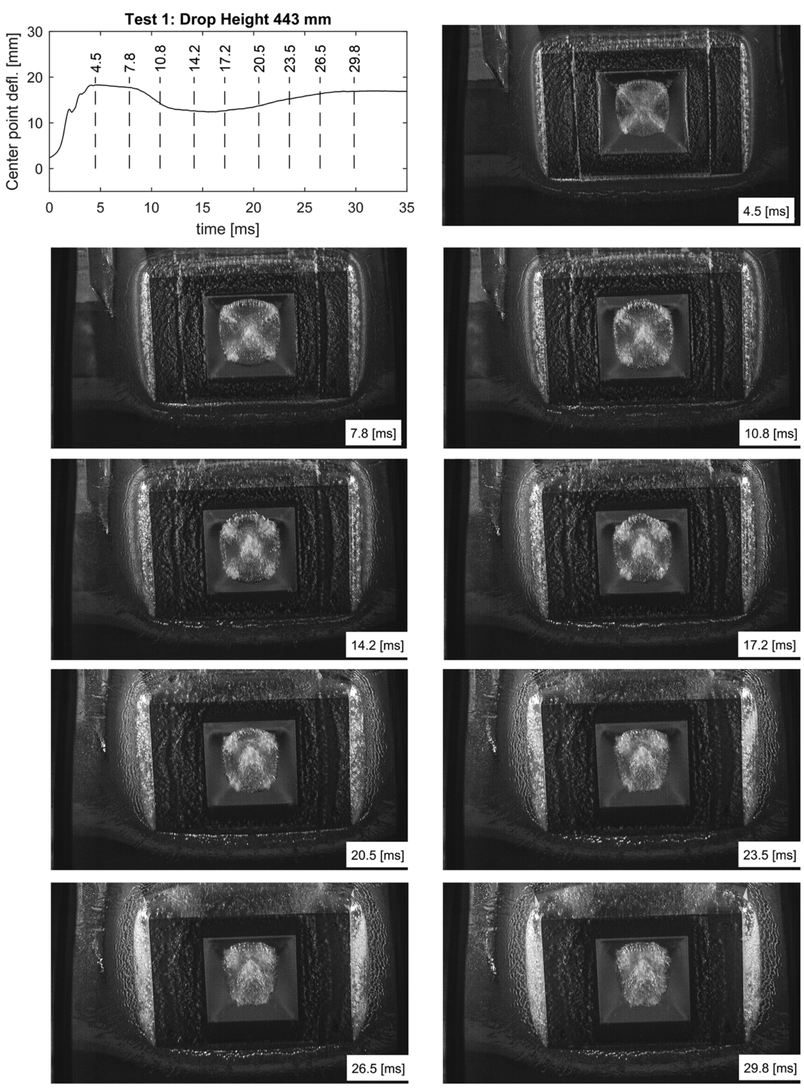

FIG. 13. High-speed images of a flat impact from a drop height of 443 mm (test 1) after extreme deformation, when the plate is deformed back and buckles along its upper edge. The positive x axis is directed downward.

plate spanned nearly the entire width of the upper boundary. The last four images show the straightening of the plate. A similar "bounce back" behavior has been observed in experiments and numerical analysis of aluminum plates subjected to air blast loading.[28,31] In this case, the plate is first subjected to a positive pressure phase followed by a negative pressure phase. These studies have shown that the magnitude of the "bounce back" depends on the timing of the negative pressure relative to that of the "bounce back" following the maximum deflection. Numerical simulations have also shown that the "bounce back" depends on the axial restraint at the boundary of the plate. The physical problem of a plate exposed to a blast load is different from that of a plate deforming due to slamming. Hence, more accurate studies are needed to better understand the "bounce back" phenomenon.

A test was also performed at a 4° angle between the plate and the free surface (test 9). The drop height was 444 mm. Figure 14 shows the synthesized high-speed video for this test.

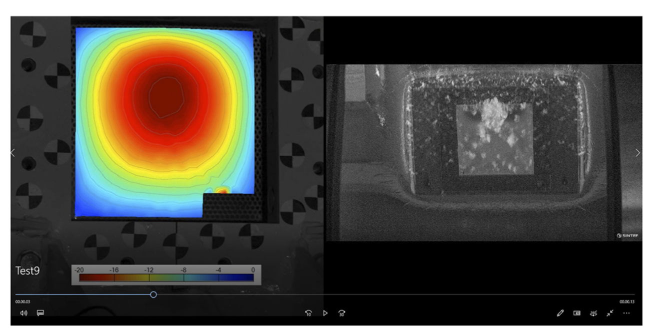

FIG. 14. Synthesized video showing images from the camera mounted above the plate and that filming the plate from below through the mirror. The colored plot on the left shows the deflection of the plate extracted using the 3D-DIC technique, and the right plot shows details of the flows of air and water beneath the plate during test 1. Multimedia view: https://doi.org/10.1063/5.0013858

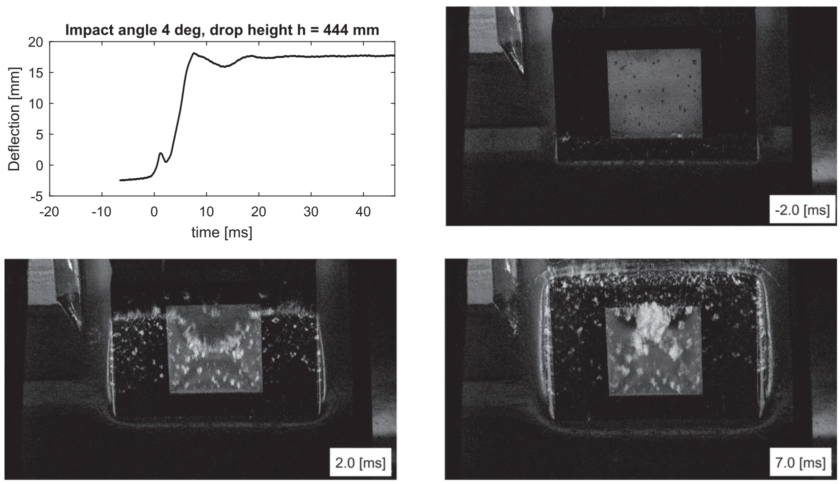

FIG. 15. High-speed images from below the plate during test 9.

Figure 15 shows images from drop test 9. The upper-left plot shows the time history of deflection at the point with the largest deflection (x = −32.5 mm, y = 2.4 mm). The time histories can be divided into three stages: (1) an initial oscillation around 2 ms, (2) rapid deformation from ∼3 ms to 8 ms, and (3) oscillation of the plate backward and out again between 8 ms and 20 ms. The images show a rapidly propagating jet crossing the plate. The deformation of the plate caused the water jet to focus at x = −55 mm and y = 0. Figure 16(a) identifies the instants when the plate was deforming quickly, and Fig. 16(b) shows deformation profiles along the x axis. The plate had large initial deformations. Contributions to the initial deformations were made by initial imperfections of the plate and heat from lamps used for the DIC recordings. This effect is further discussed in Sec. VI. The plate underwent oscillation after the initial peak of deformation. The deformation then grew until the maximum deformation occurred.

VI. ACCURACY OF DIC MEASUREMENTS

The accuracy of the 3D-DIC measurements was checked with a coordinate measuring machine (CMM). The machine consisted of an automatic robot arm with a pin that measured the surface geometry. Figure 17(a) shows a comparison of the permanent deformations of the plate along the x axis for test 1 and test 9. For both tests, the difference between the measurements was ∼0.2 mm at the point corresponding to maximum deflection.

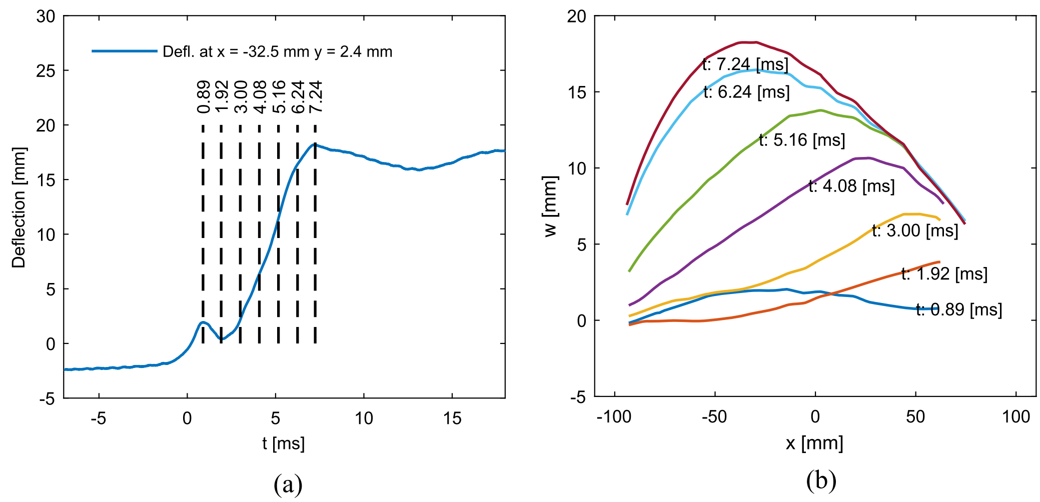

FIG. 16. (a) Plot shows the time history of deflection of the point corresponding to the maximum deflection during the stage of rapid deformation of the drop with a 4° angle between the underside of the box and the free surface. (b) Plot shows profiles of the deflection along the x axis at y = 0.

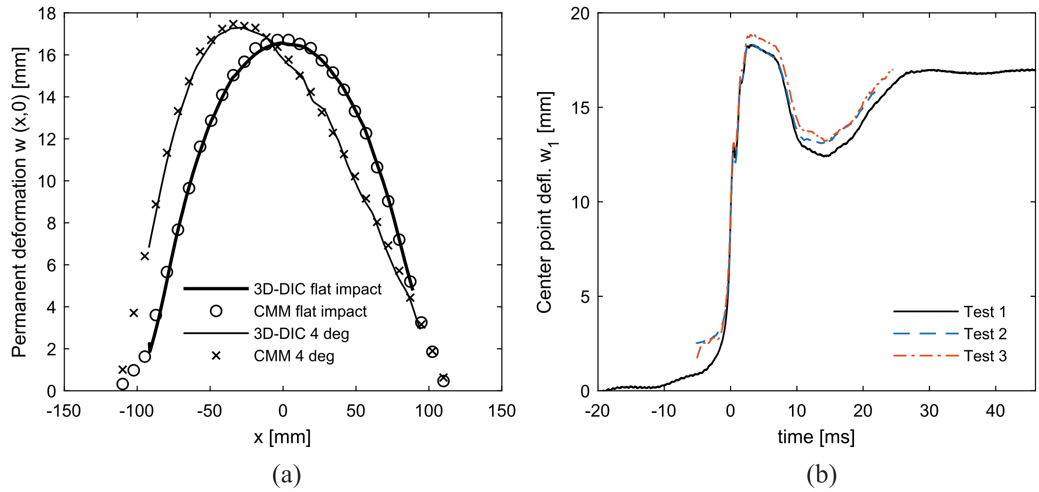

FIG. 17. (a) Plot compares permanent deformations after impact, measured using 3D-DIC and a coordinate measuring machine (CMM) (Mitutoyo). (b) Time history of deflection of the plate center for repeated tests at a drop height of 443 mm.

Figure 17(b) shows the deflection at the center in three tests from a drop height of 443 mm. Tests 2 and 3 showed initial deflections of 1.5 mm–2 mm, which was surprising as the initial deflection of the plate was checked prior to mounting the frame on the drop rig. This deflection was typically 0.5 mm. The reason for this large initial deflection was the thermal expansion of the plate due to heat from the strong lights used for the high-speed cameras. The heating of the plate by 7° showed an initial deflection of roughly 1 mm. This means that the expansion of the plate due to heat caused significant initial deformations. During test 1, the lights used to illuminate the plate were turned on before the drop to avoid heating it. Even though the initial deflections due to heating were large, the maximum deflection deviated by less than 1 mm in tests 1, 2, and 3.

VII. IMPACT VELOCITY ESTIMATED FROM CONSERVATION OF ENERGY

The impact velocity was estimated based on energy conservation during free fall. The drop height h was defined as the vertical distance between the free surface and the point to the left of the impacting surface. This point is denoted by A in Fig. 2 and was located at x_A = 2559 mm, y_A = −240 mm, z_A = 0 mm. As point A was lifted by a vertical distance h from the free surface, the arm of the drop rig rotated at angle Ψ. As the body underwent pure rotation, the radial velocity at any point was zero and the tangential velocity was $v_r = \omega r$. ω is the speed of rotation in radians per second. The kinetic energy for this rotation is

$$E_k = \frac{1}{2} I_{yy}\omega^2, \tag{16}$$

where I_{yy} is the moment of inertia of the entire drop rig relative to the pivot point, estimated to be 760.7 kg m^2. The potential energy at the beginning of the drop was

$$E_p = \bar{M} g h_G, \tag{17}$$

where $\bar{M}$ is the dry mass of the rig, g is the acceleration due to gravity, and h_G is the elevation of the center of gravity of the rotating body. The dry mass of the drop rig (rotating mass) was 136.8 kg, and the center of gravity was located at x_G = 2140 mm, y_G = −5 mm, z_G = 0 mm. The elevation h of the center of gravity due to the rotation of the rigid body Ψ is

$$h_G = r_G\big(\sin(\Psi + \theta) - \sin(\theta)\big). \tag{18}$$

Here, θ is the angle between the x_g axis and the line between the hinge point and the center of gravity when the bottom of the box was flush with the surface of water, i.e., Ψ = 0. The relationship between the rotation of the rig Ψ and the vertical distance between point A and the free surface is

$$\Psi = \operatorname{asin}\left(\frac{h_A}{r_A} + \sin(\theta_A)\right) - \theta_A. \tag{19}$$

The potential energy in Eq. (17) is set to be equal to the kinetic energy in Eq. (16) to obtain the impact velocity. The impact velocity had a small horizontal component because the hinge point was located 240 mm above the free surface. The impact velocity was defined as the magnitude of the vertical component of velocity at the center of the plate at the time of impact. The drop heights used in the model test were 118 mm, 222 mm, 443 mm, and 778 mm. The corresponding values of impact velocity calculated based on the conservation of energy were 1.61 m/s, 2.21 m/s, 3.11 m/s, and 4.11 m/s.

The hydroplastic theory derived in Sec. II was applied for a drop from a height of 443 mm and impact velocity of 3.11 m/s (test 1). The yield stress used in the hydroplastic calculations was referred to as the effective yield stress. Its values were between

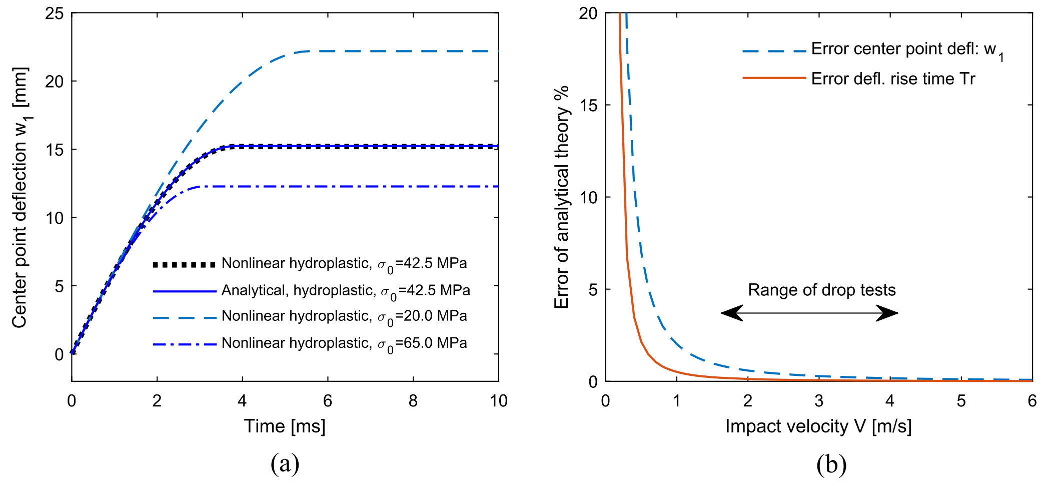

FIG. 18. Results from hydroplastic theory using the initial velocity conditions. (a) The plot shows deformation at the center at a drop height of 443 mm. (b) The plot shows error in linearizing the equation of the plate on the amplitude of deflection and rise time.

20 MPa and 65 MPa depending on the level of strain in the plate (see Fig. 5). For the calculations here, the average values of the ultimate tensile strength and yield stress were used as the effective yield stress: (20 + 65)/2 = 42.5 MPa. The uncertainty in the calculations was then investigated using the upper (65 MPa) and lower (20 MPa) values to check their sensitivity. To use hydroplastic theory, it is necessary to calculate the added mass due to oscillations of the pyramid-shaped mode. The computer program Wamit[32] was used for this purpose, and the added mass was found to be $A = 0.6$ kg.

Figure 18(a) shows the time history of the deflection of the midpoint of the plate, assuming an impact velocity of 3.11 m/s. The calculated maximum deformation was sensitive to the effective yield stress. The difference between the nonlinear hydroplastic solution and the analytical hydroplastic solution is the linearization of the structural resistance term in the latter. Figure 18(b) shows the error in the maximum deflection w_1 and the rise time of the deflection T_r due to this linearization, as a function of impact velocity. The range of drop heights studied here is indicated with a double arrow. The plot shows that the error in using the analytical hydroplastic theory, i.e., Eq. (10), was less than 2% for the peak deflection and less than 1% for the rise time of deflection. The deformations of the plate were clearly dominated by membrane action for the range of drop heights considered. Jones[19,20] claimed that membrane action is dominant when the deflection becomes larger than the thickness of the plate.

VIII. ACCURACY OF ESTIMATED IMPACT VELOCITY

The theoretical results in Fig. 18(a) used the impact velocity of 3.11 m/s as input, which was based on the conservation of energy. The black solid curve in Fig. 19 shows that the measured impact velocity based on 3D-DIC measurements was 3.04 m/s. The black dashed curve shows that based on the integration of accelerometers mounted inside the box. This latter measurement was aligned with the peak of the DIC measurements. The reduction in velocity estimated from the accelerometers and 3D-DIC compared well.

The measured deceleration during impact can be split in two parts. The first consisted of a very quick retardation from 3 m/s to 2.7 m/s over only 1.2 ms. This suggests an average acceleration of -200 m/s^2. In the second part, this quick deceleration was followed by a slower deceleration from 2.7 m/s to 2.5 m/s over 5 ms, which

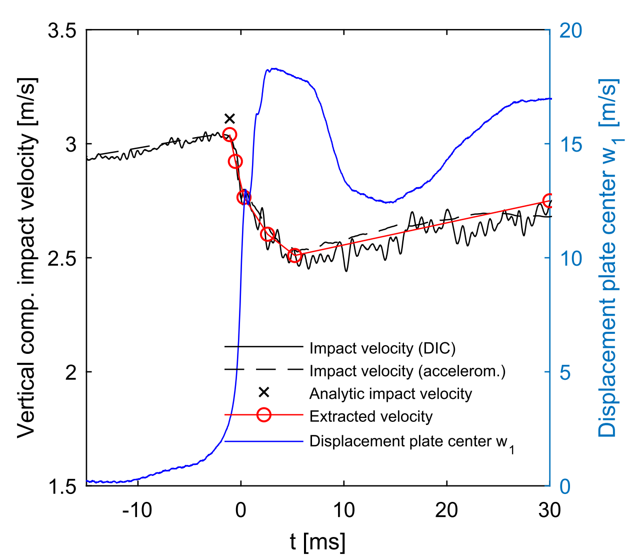

FIG. 19. The plot shows the impact velocity measured using the 3D-DIC method and accelerometers (left y axis) and the deflection of the plate (right y axis) during test 1. The plot shows uncertainty in the estimated impact velocity based on energy conservation and an ~18% reduction in velocity during impact.

suggests an average acceleration of -50 m/s^2. Figure 19 also shows no large accelerations of the box during the "bounce back" stage of the impact. This suggests that the "bounce back" was not induced by the global acceleration of the rig.

IX. HYDROPLASTIC THEORY BASED ON DIRECT FORCE INTEGRATION

Hydroplastic theory using the initial velocity condition assumes that the impact velocity is constant during impact. However, Fig. 19 shows that this was not the case for the model test. It is not straightforward to generalize this theory to allow for a time-varying impact velocity $V(t)$. The problem is now studied by the direct integration of hydrodynamic forces. To this end, we study the mathematical problem of a plate impacting a curved free surface. Figure 20 shows the plate as it impacts a free surface with radius of curvature R along the x axis. The curvature is much larger than the width of box B. The problem could then be treated using the theory of incompressible potential flow. The hydrodynamic model is like the one used to study the hydroelastic wedge by Faltinsen.[18] The velocity of the plate was averaged along each strip. This means that the velocity potential could be approximated as that under a rigid, heaving plate. The velocity potential can then be expressed as

$$\varphi = \left[-V(t) + \bar{w}(y,t)\right]\sqrt{c^2 - x^2}J(y,\kappa). \tag{20}$$

The factor $J(y, \kappa)$ was introduced to account for 3D effects in a simple way. $J(y,\kappa)$ is the ratio of the added mass for a heaving strip to the 2D added mass of this strip (see Fig. 20). The function $J(y,\kappa)$ is taken from Fig. 9 of Ref. 33. It depends on the location of the strip and the aspect ratio of the wetted surface $\kappa = 2c/L$. Furthermore, $\bar{w}(y,t)$ is the average speed of deformation of the wetted strip of the plate,

$$\bar{w}(y,t) = \frac{\dot{w}_1(t)}{c}\int_0^c \bar{N}(x,y)dx = \frac{\dot{w}_1(t)}{c}I_w(y) \approx \frac{\dot{w}_1(t)}{c}\sum_i \bar{N}(x_i,y)\Delta x. \tag{21}$$

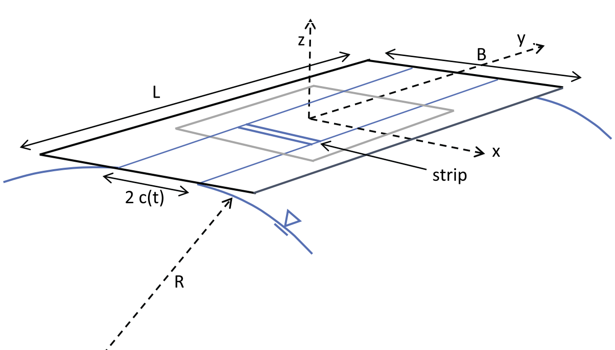

FIG. 20. Schematic of the plate impacting a wave with radius of curvature R.

The effect of the deformation on the wetted length c was neglected. The wetted length can then be determined from Wagner's theory. According to Faltinsen and Timokha,[34] the wetted length is

$$c = 2\sqrt{R\eta},\quad \dot{c} = V\sqrt{\frac{R}{\eta}}\ \text{ for }\ c \le B/2,$$
$$c = B/2,\quad \dot{c} = 0\ \text{ for }\ c > B/2, \tag{22}$$
$$\eta(t) = \int_0^t V(\tau)d\tau.$$

The pressure on the impacting surface is $p = -\rho\dot{\phi}$. Hence,

$$p = -\rho\{-\dot{V} + \dot{\bar{w}}\}\sqrt{c^2 - x^2}J(y,\kappa) - \rho\{-V + \bar{w}\}c\dot{c}\left(c^2 - x^2\right)^{-1/2}J(y,\kappa) - \rho\{-V + \bar{w}\}\sqrt{c^2 - x^2}\frac{2\dot{c}}{B}\frac{dJ(y,\kappa)}{d\kappa}. \tag{23}$$

The equation of global rotation of the drop arm is

$$I_{yy}\frac{d\omega}{dt} = -\int_S p(x_c + x)dS - \rho gLBx_c\eta + gMx_G. \tag{24}$$

The pressure given by Eq. (23) and the kinematic relationship $\omega = \dot{\eta}/x_c$ were inserted in Eq. (24). This leads to the following equation for the global rotation of the drop rig:

$$\left(\frac{I_{yy}}{x_c} + \rho I_{1g}\right)\ddot{\eta} - \rho I_{2g}\ddot{w}_1 = -\rho\dot{c}\left(cI_{3g} + \frac{2}{B}I_{5g}\right)\dot{\eta} + \rho\dot{c}\left(cI_{4g} + \frac{2}{B}I_{6g}\right)\dot{w}_1 - \rho gLBx_c\eta + gMx_G. \tag{25}$$

The integrals I_{ig}, $i = 1,2, \ldots, 6$ are listed in Eq. (27). The deformation of the plate is described by Eq. (4). Large deformations were assumed, meaning that the right-hand side of Eq. (4) was equal to $4N_0w_1\dot{w}_1$. The pressure given by Eq. (23) was inserted in Eq. (4) and leads to the following equation for the deflection of the plate:

$$-\rho I_1\ddot{\eta} + [M_s + \rho I_2]\ddot{w}_1 = \rho\dot{c}\left(cI_3 + \frac{2}{B}I_5\right)\dot{\eta} - \rho\dot{c}\left(cI_4 + \frac{2}{B}I_6\right)\dot{w}_1 - 4N_0w_1. \tag{26}$$

The integrals I_i,$i = 1,2, \ldots, 6$ are listed in Eq. (27). The time derivative of the wetted length c is infinite at $t = 0$. This means that the hydrodynamic forces in Eqs. (25) and (26) should be treated carefully. At $t = 0$, these expressions can be simplified using (1) for a small t, $\eta(t) = Vt$, which leads to $c\dot{c} = 2VR$; (2) the initial conditions $w_1 = 0$, $\dot{w}_1 = 0$, $\eta = 0$, and $\dot{\eta} = V$; and (3) the integrals calculated at $t = 0$ using $J(y,\kappa) = 1$, $dJ(y,\kappa)/d\kappa = 0$, and $I_w(y)/c = \bar{N}(0,y)$. The right column of Eq. (27) shows the integrals calculated at $t = 0$,

$$
\begin{array}{ll}
\text{Integrals for } t > 0 & \text{Integrals for } t = 0 \\
I_{1g} = x_c \int\limits_S \sqrt{c^2 - x^2} J(y,\kappa) dS & I_{1g} = 0 \\
I_{2g} = \frac{x_c}{c} \int\limits_S I_w(y) \sqrt{c^2 - x^2} J(y,\kappa) dS & I_{2g} = 0 \\
I_{3g} = x_c \int\limits_S \left(c^2 - x^2\right)^{-1/2} J(y,\kappa) dS & I_{3g} = \pi x_c L \\
I_{4g} = \frac{x_c}{c} \int\limits_S I_w(y) \left(c^2 - x^2\right)^{-1/2} J(y,\kappa) dS & I_{4g} = \pi x_c L_p \\
I_{5g} = x_c \int\limits_S \sqrt{c^2 - x^2} \frac{dJ(y,\kappa)}{d\kappa} dS & I_{5g} = 0 \\
I_{6g} = \frac{x_c}{c} \int\limits_S I_w(y) \sqrt{c^2 - x^2} \frac{dJ(y,\kappa)}{d\kappa} dS & I_{6g} = 0 \\
I_1 = \int\limits_S \bar{N}(x,y) \sqrt{c^2 - x^2} J(y,\kappa) dS & I_1 = 0 \\
I_2 = \frac{1}{c} \int\limits_S \bar{N}(x,y) I_w(y) \sqrt{c^2 - x^2} J(y,\kappa) dS & I_2 = 0 \\
I_3 = \int\limits_S \bar{N}(x,y) \left(c^2 - x^2\right)^{-1/2} J(y,\kappa) dS & I_3 = \pi L_p \\
I_4 = \frac{1}{c} \int\limits_S \bar{N}(x,y) I_w(y) \left(c^2 - x^2\right)^{-1/2} J(y,\kappa) dS & I_4 = \frac{2\pi}{3} L_p \\
I_5 = \int\limits_S \bar{N}(x,y) \sqrt{c^2 - x^2} \frac{dJ(y,\kappa)}{d\kappa} dS & I_5 = 0 \\
I_6 = \frac{1}{c} \int\limits_S \bar{N}(x,y) I_w(y) \sqrt{c^2 - x^2} \frac{dJ(y,\kappa)}{d\kappa} dS & I_6 = 0
\end{array}
\tag{27}
$$

Here, S is the wetted area of the impacting surface. The integrals were solved using numerical integration. Equations (25) and (26) were solved using a standard explicit second order Runge–Kutta time-integration procedure. A convergence test was carried out to ensure that the time steps were small enough to provide accurate solutions. As the radius if curvature of the free surface increased to infinity, the mathematical problem approached the problem of impact on a flat free surface. Equations (25) and (26) were solved for an increasing R to study this limit. The deformation at the center w_1 showed very small variations for $R > 32B$.

Figure 21 shows (1) the solution to the coupled Eqs. (25) and (26), (2) the solution to Eq. (26) assuming that the impact velocity was either constant or equal to the measured impact velocity, and (3) the analytical hydroplastic model in Eqs. (10) and (11) that assumes a constant impact velocity and a spatially averaged deflection velocity initially equal to the impact velocity. Figure 21(a) shows estimated deflections, while (b) shows the velocity of deflections and (c) shows the impact velocity for the different methods. In the calculations, the effective yield stress was $\sigma_0 = 42.5$ MPa, the half-width of the flexible plate was $L_p = 110$ mm, the horizontal coordinate of the center of the plate was $x_c = 2731$ mm, the radius of curvature of the free surface was $R = 32B$, and the impact velocity was $V(t = 0) = 3.04$ m/s.

An estimate of the effect of the deceleration of the rigid body on the deflection of the plate is the difference between the estimated maximum deflection using a constant impact velocity and the maximum deflection when using the measured impact velocity as input. The results show that the deceleration led to a reduction in the maximum deflection of about 21%. This means that if the drop test were designed such that the impact velocity was constant during impact, the expected maximum deformation would have been 21% higher than that measured.

It is also useful to compare the velocity of deformation when the plate was fully wetted with the initial velocity condition $\dot{w}_1 = 2$ V, which was used in the analytical hydroplastic theory. The comparison should be made using direct calculations where the impact velocity was constant during slamming when the plate had been fully wetted. Figure 21(b) shows that the plate's velocity was 6.75 m/s at the time, 11% higher than the velocity at the center obtained by the initial velocity condition $\dot{w}_1 = 2$ V. In comparison with the case of an elastic wedge studied by Faltinsen,[18] there was a deviation between the direct calculations and the solution based on the initial velocity condition, of 20% (see Fig. 16 of Ref. 18). The two problems are not directly comparable because of notable differences between the cases. Here, we considered the impact on a curved surface, and not a wedge with a small deadrise angle. Furthermore, this study considers plastic structural response, which means that the shape of the mode was different.

Note that the added mass used for the analytical hydroplastic method plotted in Fig. 21 was equal to $\rho I_2 = 0.48$ kg, less than the added mass calculated from Wamit, 0.6 kg. The latter value was used in Figs. 18 and 22. This deviation in the calculated added mass occurred due to the strip theory assumption of the hydrodynamic problem.

Figure 21(c) shows the impact velocity. The coupled solutions to Eqs. (25) and (26) show a quick deceleration until the plate had been fully wetted. It is interesting to compare this deceleration with that from the method by Ermanyuk and Ohkusu,[35] who studied the reduction in the velocity of a flat circular disk impacting a calm free surface. The same principles were applied to the rotating system of the drop test considered here. The rate of change in angular momentum was balanced by the moment induced by the slamming load. This can be expressed as

$$I_{yy} \frac{d\omega}{dt} = -F_s x_c. \tag{28}$$

Here, the slamming force F_s is expressed as

$$F_s = \frac{d}{dt}(A_{33} V). \tag{29}$$

The plate was assumed to be rigid, with the corresponding added mass A_{33} associated with its vertical motion. The vertical velocity was constant in space, meaning that the local rotation of the plate was neglected. The angular velocity ω and the vertical component of velocity V at the center of the plate were related as $\omega = V/x_c$. Then, the reduction in velocity at the time of impact was

$$\frac{V^+}{V^-} = \frac{I_{yy}}{I_{yy} + x_c^2 A_{33}} = 0.866. \tag{30}$$

The horizontal coordinate of the center of the plate was $x_c = 2731$ mm. The added mass was half the added mass of a thin plate in infinite fluid, as defined by Blevins,[36] $A_{33} = 15.78$ kg. For impact velocity $V^- = 3.04$, the velocity after impact was $V^+ = 2.63$ m/s. This was a larger reduction than that indicated by the coupled solution of Eqs. (25) and (26). One reason for this difference is that the deflection of the plate was not considered in Eq. (30).

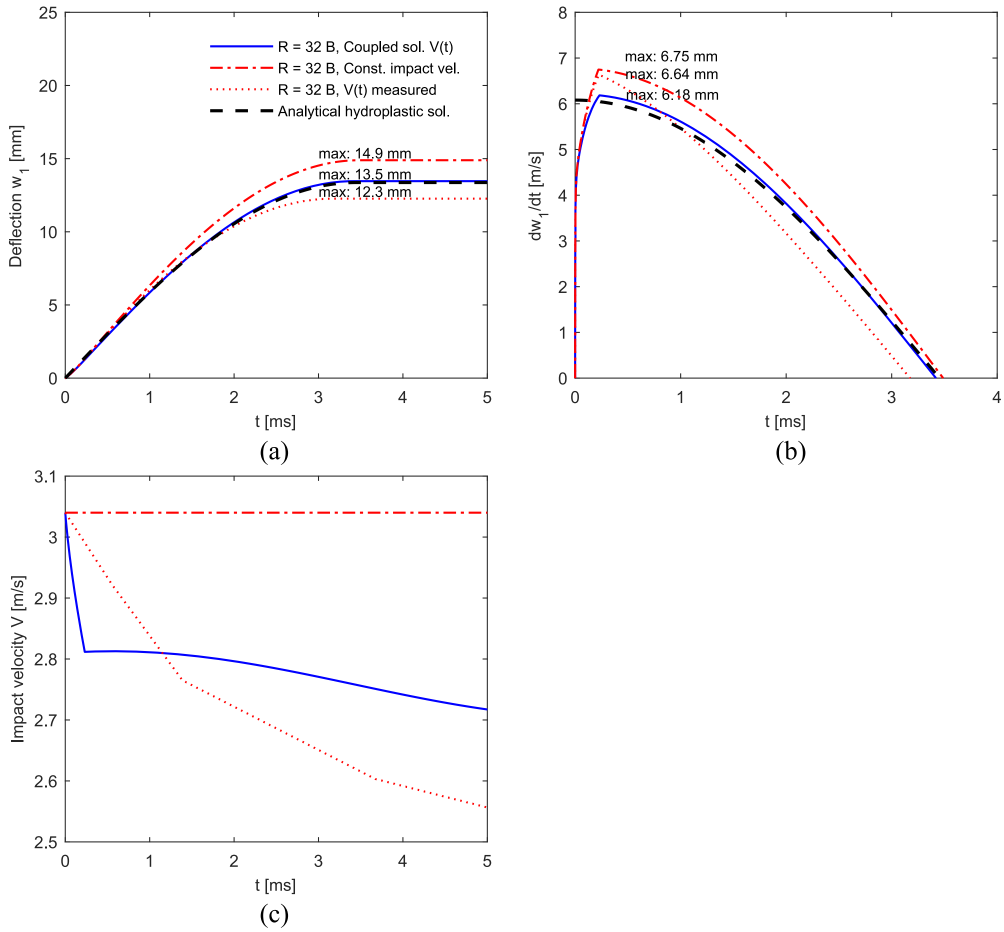

FIG. 21. Comparison between time histories of (a) deflections at the center, (b) velocity of deflection at the center, and (c) impact velocity during impact. The initial impact velocity just before impact was 3.04 m/s. The plots quantify the effects of retardation on plate deflections.

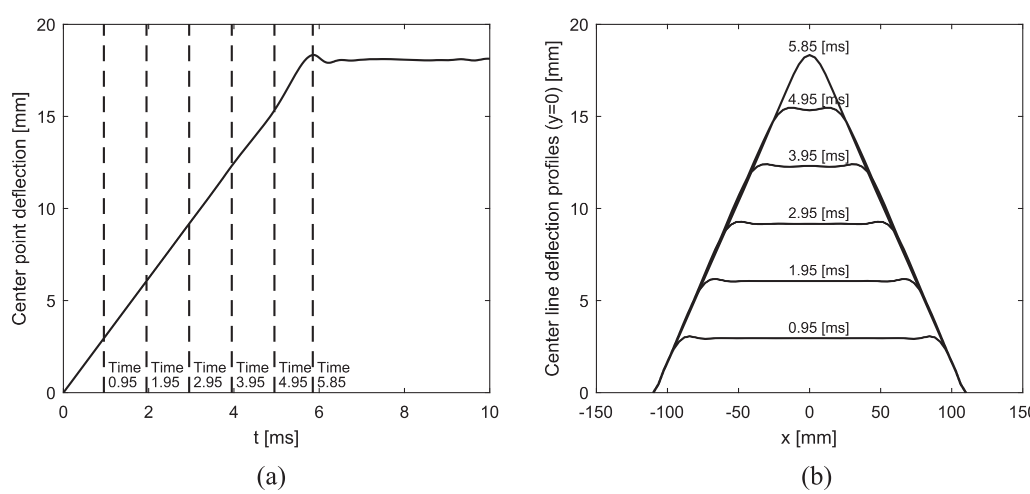

FIG. 22. FEA with an initial velocity equal to the impact velocity (3.11 m/s) for flat impact at a drop height of 443 mm. (a) Deflection in the middle of the plate as a function of time. (b) Deflection profiles for y = 0 at different instants indicated in (a). The material was defined as the modified Johnson–Cook constitutive relationship (*MAT_107), including the effect of the strain rate.

X. EFFECTS OF MATERIAL HARDENING AND STRAIN RATE

Hydroplastic theory assumes perfectly plastic behavior of the material, unlike the aluminum test plate that exhibited strain hardening (see Fig. 5). FEA simulations were therefore used to quantify the effect of strain hardening on the estimated deformations. A finite element mesh consisting of 60 × 60 square-shaped finite elements was used. At the start of the simulations, the velocity of the FEM nodes normal to the surface of the plate was set to be equal to the impact velocity. The added mass was estimated by the same Wamit analysis as applied to the hydroplastic theory described earlier. The only difference was that a piston mode shape was used to define the distribution of velocity over the plate. The added mass was modeled as point masses on the nodes of the FEM grid, and the mass was assumed to be constant during the simulation.

The FEA was carried out using the explicit solver in LS-DYNA,[24] which applies the central difference method to integrate time. The plate itself was modeled using the default Belytschko–Tsay shell elements in LS-DYNA.[24] This element applies a reduced one-point integration method to establish stress. To account for through-thickness variations in stress, nine integration points were defined along the thickness. The thinning option was further activated, which is important for membrane deformations.

Figure 22(a) shows the deformation at the center of the plate as a function of time. The plot indicates six instants. Figure 22(b) shows the deformation of the line ($y = 0$) at the same instants. The plot indicates traveling hinges moving toward the center of the plate during its deformation. The material was assumed to deform under adiabatic conditions following the modified Johnson–Cook constitutive relationship (*MAT_107) using the parameters defined in Sec. IV.

XI. COMPARISON BETWEEN THE MATHEMATICAL MODEL, FINITE ELEMENT MODEL, AND THE EXPERIMENTAL TEST RESULTS

In this section, the results of the hydroplastic and finite element methods are compared with those of the experiments. Figure 23 compares center deflections obtained using the analytical hydroplastic theory with the initial velocity condition, hydroplastic theory based on direct pressure integration, and FEA using the initial velocity condition and experiments. The plots show results of hydroplastic theory (blue curves) for three values of the yield stress, i.e., 20 MPa, 42.5 MPa, and 65 MPa.

The peak deflection from the coupled analysis using Eqs. (25) and (26) was slightly smaller than the results of the analytical hydroplastic theory using the initial velocity condition. The FEA was simulated with and without the effect of the strain rate.

The plots in Fig. 23 show that the measured deformation velocity of the center differed significantly from the impact velocity. Figure 24 shows a comparison of the deformation velocity divided by the impact velocity, $\dot{w}/V_0$, as predicted and measured for drop test 1. The measured deformation velocity at the middle of the plate was more than four times higher than the impact velocity. The plot also shows the nondimensional, spatially averaged deformation velocity for (1) the line y = 0 for the center of the plate $|x| < 80$ mm and (2) the center square area of 160 × 160 mm^2 of the plate. Both these spatially averaged deflection velocities exceeded the impact velocity. Figure 24 also shows the deformation velocity of the center of the plate, estimated using hydroplastic theory and the FEA. The plot shows a large discrepancy between the theoretical estimates and the experimental measurements.

We now consider the physical mechanism that caused large oscillations in the deflection velocity during the rapid deflection stage of the slam. Abrahamsen and Faltinsen[37] established a mathematical model of an air pocket trapped between a wave and the upper corner of a sloshing tank. The impact velocity was assumed to be constant, and the mathematical problem was hence valid for 3D flow conditions. Here, this model is extended to account for structural deformations. Water was assumed to be incompressible. The velocity potential describing the flow of water was $\phi = Vy + \phi_1(x, y) + C(t)\phi_2(x, y)$. The velocity potentials ϕ_1 and ϕ_2 satisfied the boundary value problems described in detail in Ref. 37. Water flow was connected to the air pocket through a pressure condition on the interface $p = -\rho\dot{C}(t)$. The air pocket was assumed to be closed, and its compression was assumed to be adiabatic. The dynamic pressure in the air pocket was

$$p(t) = p_0\left\{\left(\frac{\Omega_0}{\Omega(t)}\right)^{\gamma} - 1\right\}. \tag{31}$$

Here, Ω is the volume of the air pocket, Ω_0 is the initial volume of the gas pocket, γ is the ratio of specific heat, and p_0 is atmospheric pressure. The air pocket was assumed to cover the entire area of the plate. Based on the derivations in Sec. II, the equilibrium equation of the plate is as follows:

$$M_s\ddot{w}_1 + 4N_0w_1 = \frac{4}{3}L^2p. \tag{32}$$

The equation describing the rate of change in the volume of the air pocket was modified compared with Ref. 37 to account for structural deformations. The rate of change of this volume is

$$\dot{\Omega} = \dot{w}_1\int_{s_1}\bar{N}(x,y)dS - \int_{s_2}\phi_n dS. \tag{33}$$

The vertical velocity of the interface between the air pocket and water was approximated to be spatially constant, according to Faltinsen and Timokha[34] (p. 511). The hydrodynamic pressure on the interface was approximately $p(t) = -A_{33}\ddot{w}_2/(4a^2)$. Here, A_{33} was the added mass coefficient associated with the vertical motion of a piston, with the size of the air pocket embedded into a rigid plate with dimensions $L \times B$, and a is the half-width of the square-shaped air pocket. This simplification also means that the last integral in Eq. (33) is equal to $-4a^2\dot{w}_2$.

This mathematical problem was solved using a standard explicit Runge–Kutta time-integration procedure. The input to the analysis was taken from test 1. The volume of the air pocket was estimated at the time of maximum deflection using a combination of the high-speed video and the 3D-DIC measurements. The volume of the air pocket in drop test 1 was $\Omega_0 = 5.4 \times 10^{-5}$ m^3. The half-width of the air pocket was $a = 53$ mm. The added mass $A_{33} = 0.49$ kg was calculated using Wamit.[32] The ratio of specific heat of air was $\gamma = 1.4$, atmospheric pressure was 1.01×10^5 Pa, and the effective

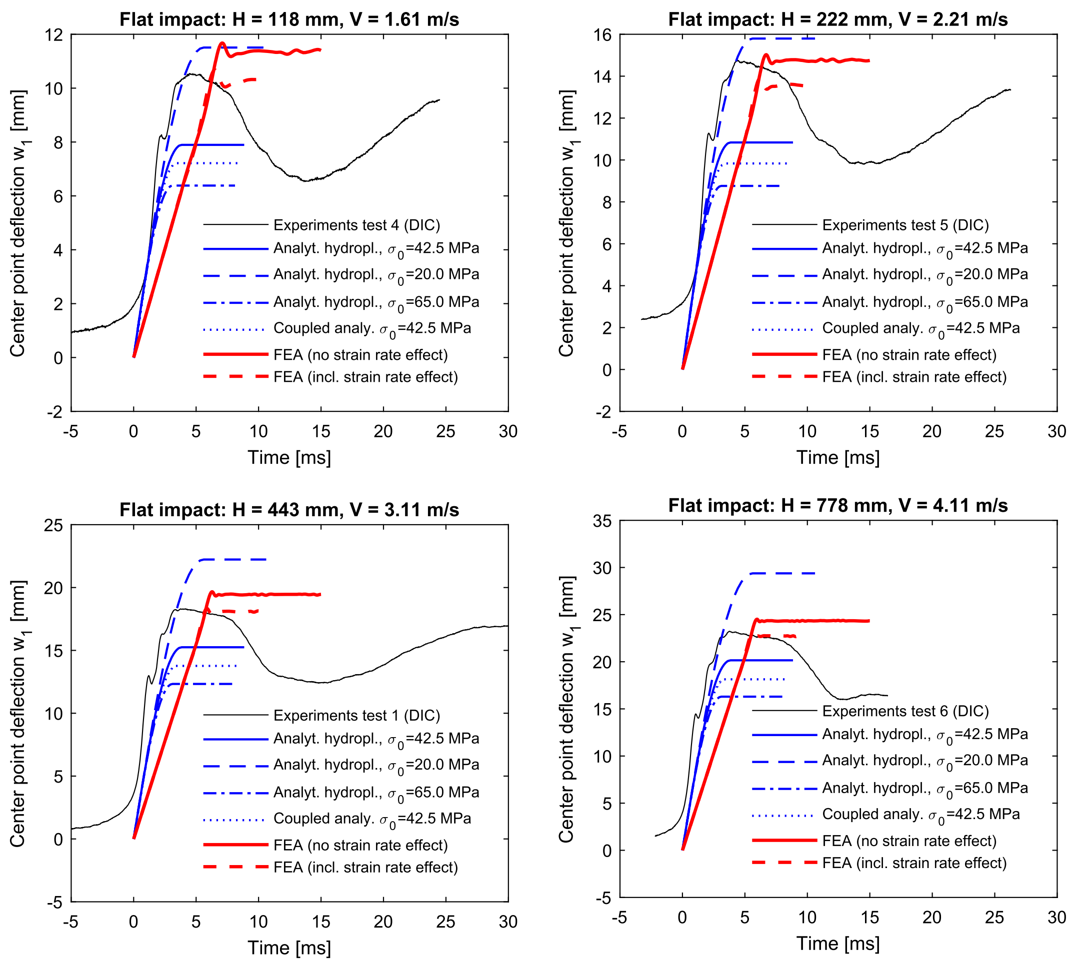

FIG. 23. Comparison of midpoint deflections based on DIC measurements, hydroplastic theories, and FEA for the drops at heights of 118 mm, 222 mm, 443 mm, and 778 mm.

yield stress was 42.5 MPa. The initial conditions for the numerical integration were $w_1 = 0$, $\dot{w}_1 = 0$, $w_2 = 0$, $\dot{w}_2 = 3.11$ m/s, and $\Omega_0 = 5.4 \times 10^{-5}$ m^3 at t = 0.

Figures 25(a) and 25(b) show displacements and velocities of the plate and the air pocket during the impact, resulting from the numerical integration of the problem. The time series of the deflection of the plate exhibited deformations at two distinct timescales. The first was the slow timescale, which has already been described well using the analytic hydroplastic theory derived in Sec. II. The second was a shorter timescale with a period of ~1.1 ms. Response at this timescale was visible only in the deflection of the plate, and not in the motion of the interface between air and water. This suggests that the timescale of these oscillations can be identified by setting $w_2 = 0$, if the pressure–volume relationship in Eq. (31) can be linearized by assuming fluctuations of small volume; $p = p_0\gamma(\Omega_0 - \Omega)/\Omega_0$, as in Ref. 38. Inserting this expression into Eq. (32), and neglecting the motion of the interface between water and air in Eq. (33), the following natural frequency can be derived:

$$\omega^2 = \frac{4N_0 + \frac{4L_p^2 p_0 \gamma I_{AP}}{3\Omega_0}}{M_s}. \tag{34}$$

Here, I_{AP} is equal to the first integral in Eq. (33). Inserting the same input as used in Fig. 25 (test 1), Eq. (34) estimates a natural period of 1.1 ms. Equation (32) is valid only if the velocity of deflection is positive. Figure 24 shows that the duration of the first half-cycle of the deflection velocity is approximately half the period calculated from Eq. (32). This means that the oscillations in the velocity of deflection experienced during the rapid deformation stage of the impact likely occurred owing to the free vibrations of the plate on top of the air pocket. The mass was then associated with the mass of the plate, and stiffness was associated with the compressibility of the air pocket and the resistance of the plate.

The aim of the scaled experiment was to obtain geometrically scaled plate deflections for a 0.6-mm aluminum plate and an

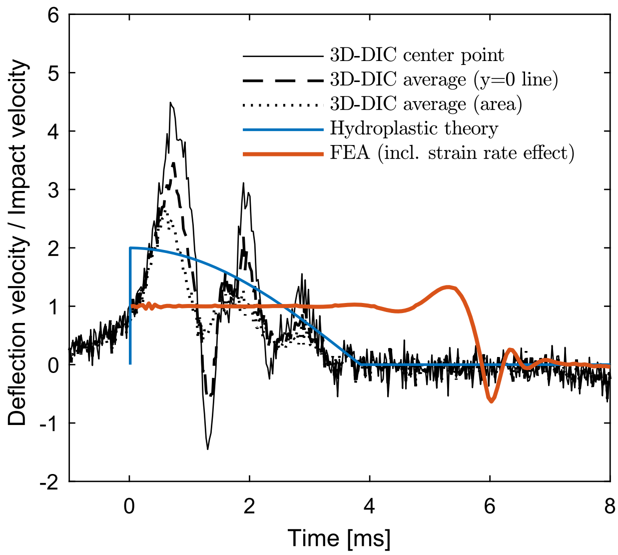

FIG. 24. Deformation velocity divided by the impact velocity for 3D-DIC, hydroplastic theory, and FEA results at a drop height of 443 mm. For the 3D-DIC measurements, three estimates were plotted: (1) $\dot{w}$ is the speed of deformation of the center. (2) $\dot{w}$ is the average speed of deformation of the middle section y = 0 from x = −80 to x = 80 mm. (3) $\dot{w}$ is the average speed of deformation of the plate in the square area from x = y = −80 mm to x = y = 80 mm. For hydroplastic theory and the FEA, $\dot{w}$ is the velocity at the center.

18-mm steel plate at a scale of 1:14.5. The scaling is based on Eq. (11) where the physics of the entrapped air cushion was neglected. Hence, the coupled air pocket model [Eqs. (31)–(33)] can be used to discuss the validity of the scaling. The definition of the velocity potential just prior to Eq. (31) shows that $p/(\rho V^2)$ was the relevant nondimensional pressure. Dividing Eq. (31) by ρV^2 shows that the Euler number $p_0/(\rho V^2)$ was a parameter in the problem. Furthermore, a nondimensional version of Eq. (32) yields the nondimensional mass, $M_s/(\rho L_p^3)$, and nondimensional structural resistance, $N_p/(\rho L_p V^2)$. Only the structural resistance was scaled correctly. The physics associated with the Euler number has been discussed in Refs. 34 and 37 in connection with oscillating air pockets trapped by gravitational waves inside tanks with rigid walls. In this case, the pressure inside the air pocket does not follow Froude's scaling if the Euler numbers are different between the model and the full-scale problem. However, even if the Euler numbers are different, the time integral of pressure, i.e., the impulse, still followed Froude's scaling. As the Euler number and the nondimensional mass were different between the model and the full-scale problem studied here, the mechanism causing rapid oscillations in velocity in Fig. 24 is not expected to be similar in model and full scale. However, the physics of the pressure oscillations inside the air pocket causing the velocity fluctuations of the plate is secondary to the physics described by Eq. (11), which was the basis for scaling the experiment. Other physics that is not handled by the scaled experiment is the viscous effects. However, since viscous flow separation does not occur in the water, the viscous effects will only be present in the boundary layer flow at the solid body. Since associated shear stresses are small relative to pressures, we can neglect the viscous effects in water. Finally, surface tension effects were not accounted for in the scaled experiment. Surface tension matters for small stable air bubbles in water and balances the pressure inside the air bubble. However, even for small air bubbles of order 1 mm in size, the surface tension does not affect the natural frequency of the air bubble (see, for instance, Ref. 39, p. 186). Hence, since the air pocket entrapped in the experiment is orders of magnitude larger than this, the physical behavior of the air pocket is not believed to be influenced by surface tension effects.

Figure 26 shows the maximum deformation of the plate as a function of impact velocity. Both the permanent deformation measured with a dial gauge and the maximum deflection from the DIC measurements are shown. Figure 26(a) shows a comparison between

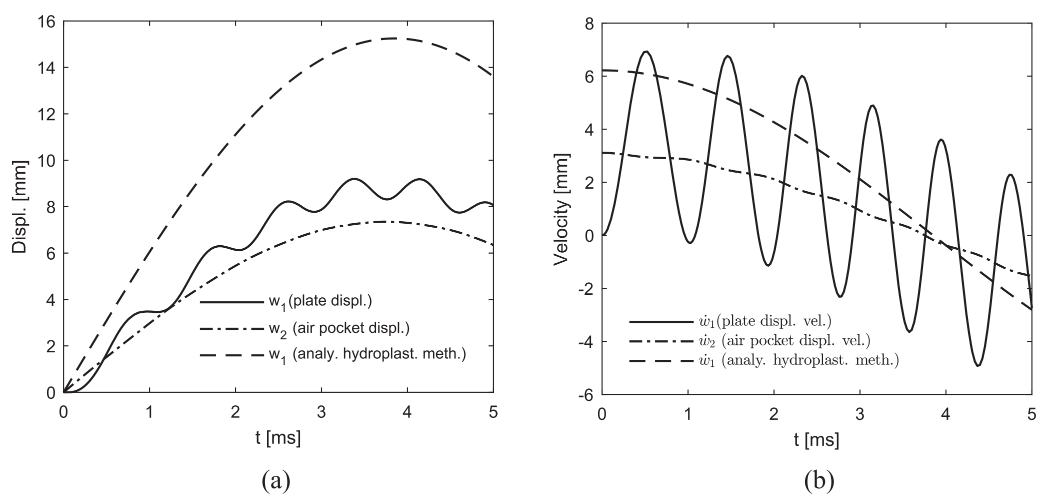

FIG. 25. Time histories of (a) deformations and (b) velocities of the plate and air pocket during impact.

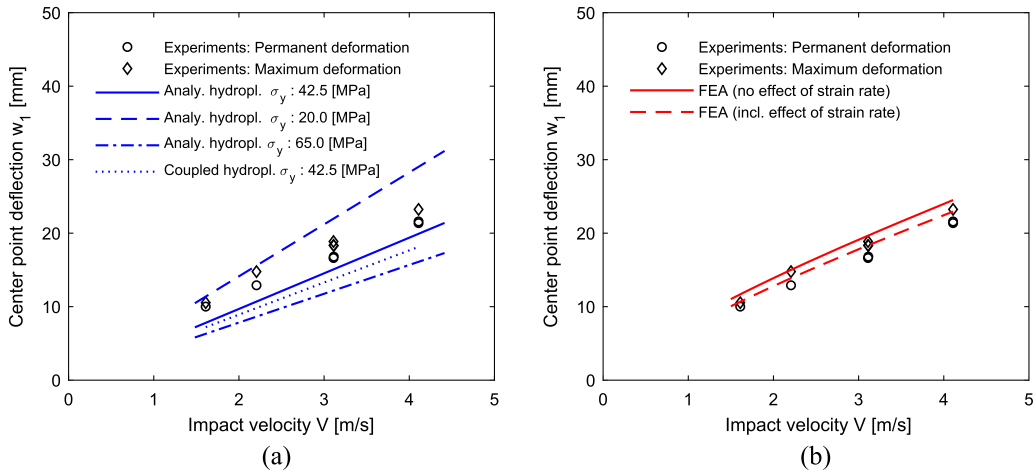

FIG. 26. Comparison of maximum deflections of the plate during flat impact at different impact velocities. (a) Hydroplastic theory and experimental results. (b) FEA using the model of material with and without the effects of the strain rate.

these sets of experimental data, with the maximum deformations from analytical hydroplastic theory obtained using three values for the yield stress: 20 MPa, 45 MPa, and 65 MPa. All experimental peaks were between the theoretical curves, with a yield stress ranging from 20 MPa to 45 MPa. The results of analytical hydroplastic theory assumed a yield stress of 65 MPa to show low estimates of the maximum deformation.

Figure 26(b) shows a comparison in terms of the maximum deflection between the FEA and the experiments. It shows the results of the FEA with and without the effects of the strain rate, which was about 10% at peak deflection. The effect of the strain rate might be more significant than this in the model test, given that the measured deflection velocity of deformation was higher than that in the analysis.

The hydroplastic theory shows that the maximum deformation was linearly dependent on velocity. The results of the FEA showed a slight deviation from a straight line. One reason for this difference might have been the strain hardening of the material. It is not clear whether the experimental measurements showed the same trend.

Figure 27 shows a comparison of the deflection profiles along the x axis at a drop height of 443 mm at the time corresponding to the peak deflection. The shape of deflection was triangular according to hydroplastic theory and was nearly triangular for the results of the FEA. However, the profile of experimental deflection corresponded closely to the shape of a cosine mode. Experience from air blast loading on aluminum and steel plates shows that the duration of the load alters the shape of deflection, from pyramid shaped, for a load imposed for a short duration,[28] to a more cosine-shaped deflection, for a load imposed for longer time.[40] Furthermore, the aluminum alloy used in the drop tests showed significant strain hardening for the magnitudes of strain considered. Strain hardening tends to distribute plasticity on a larger area of the plate.[41] This may explain the difference between the analytical hydroplastic theory and the results of the FEA in Fig. 27. The aim of the mathematical analysis carried out here was to design and analyze errors in the drop test. More elaborate analysis, which fully accounts for the combined aero- and hydro-structural physics, is necessary for a deeper insight into the physics of the observed cosine shape of deflection.

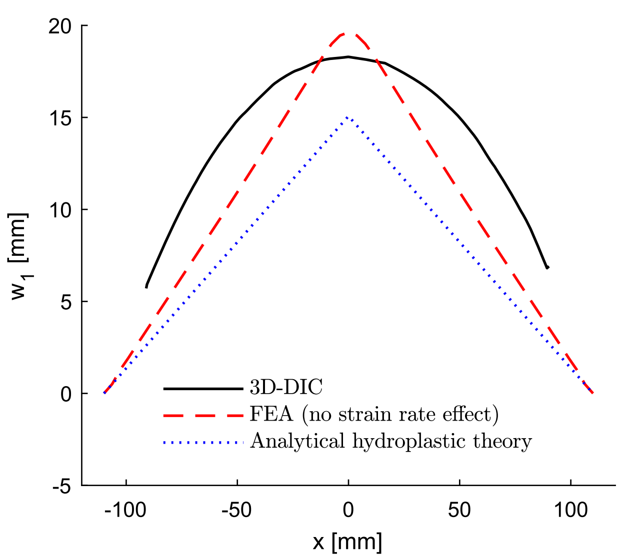

FIG. 27. Comparison of the shape of deflection at maximum deflection for different methods at a drop height of 443 mm.

XII. CONCLUSIONS

The drop tests described here were designed to study large and plastic deformations of a square plate, with equal emphasis on its structural mechanics and hydrodynamics. Dual cameras were used to monitor the deforming plate from above, and the deformations were tracked using the 3D-DIC technique developed in Refs. 21 and 22. The complex hydrodynamics of the impact were captured with a high-speed camera from below. The design of the frame holding the deformable plate was inspired by setups used for explosion testing, where the plate is clamped between thick frames.[28] The new design leaves the area in front of the plate flush, while its edges are close to fixed along the four boundaries.

During flat impact, the plate developed large plastic deformations. In the experiments, the maximum deformations ranged from 16 to 38 times the thickness of the plate. The plate deformed into a cosine deflection shape. The high-speed video filming the plate from below during the impact showed the entrapment of a large air pocket that covered roughly 50% of it during impact. Drop tests with stiffer plates showed much less air trapped beneath the plate. This shows that the amount of air trapped depends on the stiffness of the plate. The types of air pockets studied here have, to the knowledge of the authors, not been described in the literature in the area to date.

The proposed analytical hydroplastic theory expands the hydroelastic theory proposed by Faltinsen[14] using the rigid plastic analysis by Jones.[19,20] The method solves for the free vibration of a nonlinear, single-degree equation of freedom with an initial velocity condition like that in the hydroelastic theory proposed by Faltinsen. Analytical hydroplastic theory shows that the deflection in amplitude at the center is proportional to the impact velocity. When the deformation of the plate is dominated by membrane action, the analysis can be linearized and an analytical solution can be obtained. Comparisons between the measured and estimated deflections using analytical hydroplastic theory show that it can adequately capture the maximum/permanent deflections of the plate. However, shapes of the theoretical deflection form a pyramid, while the experiments show a cosine shape of deflection.

Drop tests at a height of 443 mm were repeated three times to check for repetition error. The maximum deformation was within ±2.5%. The DIC measurements were compared with those from a coordinate measurement machine (CMM). The errors were along the order of 1% and might have been due to a difference in temperature between the location of the drop test and that of the CMM apparatus. The impact velocity of the rig was estimated using the principle of energy conservation. For drop test 1, the theoretical estimate of impact velocity was 2% higher than the experimentally measured value. Furthermore, for this test, the deceleration in the rig until the maximum deformation of the plate was 15% of the initial impact velocity.

The effect of deceleration on the deformation of the plate was investigated through a separate mathematical model. The plate was assumed to impact a curved free surface. As the curvature increased to infinity, the problem then became equivalent to that of the impact on a flat free surface when the air underneath the plate is neglected. The numerical model directly integrated the equations of equilibrium of the plate with the hydrodynamic pressure model based on Wagner's theory.[1] The analysis showed that the deceleration of the rig during the impact led to a reduction in the maximum deflection of 21%. The model was also used to assess the validity of the initial velocity conditions used in the analytical hydroplastic method. The numerical model based on direct integration yielded an initial velocity of 11% higher than that used in the analytical hydroplastic method.

The aluminum alloy used for the experiments (A1050 H111) exhibited considerable strain hardening, which means that the definition of the effective yield stress used as input to the hydroplastic theories was uncertain. The maximum midpoint deflection was relatively accurately estimated using the average value between the first and the ultimate tensile yield strengths of the aluminum plate. The finite element method was used to study the effect of a more accurate material model on the structural response. The FEA model provided good agreement with the DIC measurements in terms of center deflection. The effect of the strain rate on the FEA amounted to a 10% reduction in the peak deflection for the studied impacts.

The FEA and the analytical hydroplastic theory assume that the spatially averaged velocity of deflection is equal to the impact velocity. However, the experiments here showed that the spatially averaged deflection velocity is approximately twice that and oscillates during impact. Given that both the FEA and the analytical hydroplastic theory neglected the influence of the air pocket, the coupled water–air pocket-structure physics was studied. A simplified two-degree-of-freedom model representing the deflections of the plate and the compression of air pocket was established and solved numerically. The first-half period of the measured deflections was comparable to half the period estimated from the numerical model. The result suggests that the oscillations in deflection velocity during the slam were due to the free vibration of the plate on top of the air pocket. The mass can then be associated with the mass of the plate, and stiffness can be associated with the compressibility of the air pocket and resistance of the plate.

The experiments here show that the plate was pushed down and then up after the time of maximum deflection. This "bounce back" behavior is not reproduced by hydroplastic theory, nor is it present in the FEA presented here. The measurements show that global accelerations of the drop arm were small during the time of the "bounce back." Hence, this bounce back does not seem to be directly caused by global acceleration. More accurate models are needed to understand the physics of this phenomenon.

ACKNOWLEDGMENTS

This study was supported by Equinor, Aker Solutions, and Multiconsult through the SLADE Pilot JIP; the Research Council of Norway, Equinor, Aker Solutions, Multiconsult, Kværner, and the Norwegian Shipowners Association through the SLADE KPN project (RCN Project No. 294748); the Centre of Autonomous Marine Operations and Systems (AMOS–RCN Project No. 223254); the Centre for Advanced Structural Analysis (CASA–RCN Project No. 237885); and the Norwegian Ministry of Justice and Public Security.

DATA AVAILABILITY

The data that support the findings of this study are available from the corresponding author upon reasonable request.

REFERENCES

[1] H. Wagner, "Über Stoß- und gleitvorgänge an der oberfläche von flüssigkeiten," Z. Angew. Math. Mech. **12**(4), 193–215 (1932).

[2] A. Korobkin, "Blunt-body impact on a compressible liquid surface," J. Fluid Mech. **244**, 437–453 (1992).

[3] A. Korobkin, "Analytical models of water impact," Eur. J. Appl. Math. **15**(6), 821–838 (2004).
[4] R. Zhao and O. Faltinsen, "Water entry of two-dimensional bodies," J. Fluid Mech. **246**, 593–612 (1993).
[5] S. L. Chuang, "Experiments on flat-bottom slamming," J. Ship Res. **10**, 10–17 (1966).
[6] J. H. G. Verhagen, "The impact of a flat plate on a water surface," J. Ship Res. **11**(4), 211–223 (1967).
[7] B. R. Koehler and C. F. Kettleborough, "Hydrodynamic impact of a falling body upon a viscous incompressible fluid," J. Ship Res. **21**, 165–181 (1977).
[8] H. C. Mayer and R. Krechetnikov, "Flat plate impact on water," J. Fluid Mech. **850**, 1066–1116 (2018).
[9] C. H. Lu, Y. S. He, and G. X. Wu, "Coupled analysis of nonlinear interaction between fluid and structure during impact," J. Fluid Struct. **14**, 127–146 (2000).
[10] T. I. Khabakhpasheva and A. A. Korobkin, "Elastic wedge impact onto a liquid surface: Wagner's solution and approximate models," J. Fluid Struct. **36**, 32–49 (2013).
[11] A. Shams, S. Zhao, and M. Porfiri, "Hydroelastic slamming of flexible wedges: Modelling and experiments from water entry to exit," Phys. Fluids **29**, 037107 (2017).
[12] S. Okada and Y. Sumi, "On the water impact and elastic response of a flat plate at small impact angles," J. Mar. Sci. Technol. **5**, 31–39 (2000).
[13] O. M. Faltinsen, J. Kvålsvold, and J. V. Aarsnes, "Wave impact on a horizontal elastic plate," J. Mar. Sci. Technol. **2**, 87–100 (1997).
[14] O. M. Faltinsen, "The effect of hydroelasticity on ship slamming," Philos. Trans. R. Soc. London. A **355**, 575–591 (1997).
[15] A. Korobkin, "Wave impact on the center of an Euler beam," J. Appl. Mech. Tech. Phys. **39**, 770 (1998).
[16] Z. Yu, J. Amdahl, M. Greco, and H. Xu, "Hydro-plastic response of beams and stiffened panels subjected to extreme water slamming at small impact angles, Part I: An analytical solution," Mar. Struct. **65**, 53–57 (2019).
[17] Z. Yu, J. Amdahl, M. Greco, and H. Xu, "Hydro-plastic response of beams and stiffened panels subjected to extreme water slamming at small impact angles, Part II: Numerical verification and analysis," Mar. Struct. **65**, 114–133 (2019).
[18] O. M. Faltinsen, "Water entry of a wedge by hydroelastic orthotropic plate theory," J. Ship Res. **43**, 180–193 (1999).
[19] N. Jones, "A theoretical study of the dynamic plastic behavior of beams and plates with finite-deflections," Int. J. Solid Struct. **7**, 1007–1029 (1971).
[20] N. Jones, "Influence of in-plane displacements at the boundaries of rigid-plastic beams and plates," Int. J. Mech. Sci. **15**, 547–561 (1973).
[21] See https://www.ntnu.edu/kt/ecorr for eCorr user manual.
[22] E. Fagerholt, "Field measurements in mechanical testing using close-range photogrammetry and digital image analysis," Ph.D. thesis, Norwegian University of Science and Technology, NTNU, Norway, 2012.
[23] E. Fagerholt, T. Børvik, and O. S. Hopperstad, "Measuring discontinuous displacement fields in cracked specimens using digital image correlation with mesh adaptation and crack-path optimization ," Opt. Laser Eng. **51**, 299–310 (2013).
[24] See http://www.lstc.com for Livermore Software Technology Corporation (LSTC); cited 13.12.18.
[25] T. Børvik, O. S. Hopperstad, T. Berstad, and M. Langseth, "A computational model of viscoplasticity and ductile damage for impact and penetration," Eur. J. Mech. A **20**, 685–712 (2001).
[26] D. K. Christoulis, S. Guetta, V. Guipont, and M. Jeandin, "The influence of the substrate on the deposition of cold-sprayed titanium: An experimental and numerical study," J. Therm. Spray Technol. **20**, 523–533 (2011).
[27] M. A. Louar, B. Belkassem, H. Ousji, K. Spranghers, L. Pyl, and J. Vantomme, "Estimation of the strain rate hardening of aluminium using an inverse method and blast loading," J. Dyn. Behav. Mater. **3**, 347–361 (2017).
[28] V. Aune, E. Fagerholt, K. O. Hauge, M. Langseth, and T. Børvik, "Experimental study on the response of thin aluminium and steel plates subjected to airblast loading," Int. J. Impact Eng. **90**, 106–121 (2016).
[29] DNV-RP-C208, Determination of structural capacity by non-linear FE analysis methods, June 2013.
[30] I. Watanabe, K. Tanizawa, and H. Sawada, "An observation of bottom impact phenomena by means of high speed video and transparent model," Nav. Archit. Ocean Eng. **27**, 35–42 (1989).
[31] V. Aune, G. Valsamos, F. Casadei, M. Larcher, M. Langseth, and T. Børvik, "Numerical study on the structural response of blast-loaded thin aluminium and steel plates," Int. J. Impact Eng. **99**, 131–144 (2017).
[32] See www.wamit.com for WAMIT user manual.
[33] W. K. Meyerhoff, "Added masses of thin rectangular plates calculated from potential theory," J. Ship Res. **14**, 100–110 (1970).
[34] O. M. Faltinsen and A. N. Timokha, *Sloshing* (Cambridge University Press, 2009).
[35] E. V. Ermanyuk and M. Ohkusu, "Impact of a disk on shallow water," J. Fluid Struct. **20**, 345–357 (2005).
[36] R. D. Blevins, *Formulas for Natural Frequency and Mode Shape* (Krieger Publishing Company, 2001).
[37] B. C. Abrahamsen and O. M. Faltinsen, "Scaling of entrapped gas pocket slamming events at dissimilar Euler number," J. Fluid Struct. **40**, 246–256 (2013).
[38] B. C. Abrahamsen and O. M. Faltinsen, "The natural frequency of the pressure oscillations inside a water-wave entrapped air pocket on a rigid wall," J. Fluid Struct. **35**, 200–212 (2012).
[39] T. G. Leighton, *The Accoustic Bubble* (Academic, London, 1994).
[40] V. Aune, E. Fagerholt, M. Langseth, and T. Børvik, "A shock tube facility to generate blast loading on structures," Int. J. Prot. Struct. **7**(3), 340–366 (2016).
[41] H. Granum, V. Aune, T. Børvik, and O. S. Hopperstad, "Effect of heat-treatment on the structural response of blast-loaded aluminum plates with pre-cut slits," Int. J. Impact Eng. **132**, 103306 (2019).